Understanding the Equatorial Pacific Cold Tongue Time-Mean Heat Budget. Part II: Evaluation of the GFDL-FLOR Coupled GCM

SULAGNA RAY

Atmospheric and Oceanic Sciences Program, Princeton University, Princeton, New Jersey

ANDREW T. WITTENBERG, STEPHEN M. GRIFFIES, AND FANRONG ZENG

National Oceanic and Atmospheric Administration/Geophysical Fluid Dynamics Laboratory, Princeton, New Jersey

ABSTRACT

The heat budget of the Pacific equatorial cold tongue (ECT) is explored using the GFDL-FLOR coupled GCM (the forecast-oriented low ocean resolution version of CM2.5) and ocean reanalyses, leveraging the two-layer framework developed in Part I. Despite FLOR's relatively weak meridional stirring by tropical instability waves (TIWs), the model maintains a reasonable SST and thermocline depth in the ECT via two compensating biases: 1) enhanced monthly-scale vertical advective cooling below the surface mixed layer (SML), due to overly cyclonic off-equatorial wind stress that acts to cool the equatorial source waters; and 2) an excessive SST contrast between the ECT and off-equator areas, which boosts the equatorward heat transport by TIWs. FLOR's strong advective cooling at the SML base is compensated by strong downward diffusion of heat out of the SML, which then allows FLOR's ECT to take up a realistic heat flux from the atmosphere. Correcting FLOR's climatological SST and wind stress biases via flux adjustment (FA) leads to weaker deep advective cooling of the ECT, which then erodes the upper-ocean thermal stratification, enhances vertical mixing, and excessively deepens the thermocline. FA does strengthen FLOR's meridional shear of the zonal currents in the east Pacific, but this does not amplify either the simulated TIWs or their equatorward heat transport, likely due to FLOR's coarse zonal ocean resolution. The analysis suggests that to advance coupled simulations of the ECT, improved winds and surface heat fluxes must go hand in hand with improved subseasonal and parameterized ocean processes. Implications for model development and the tropical Pacific observing system are discussed.

1. Introduction

Excessively cold sea surface temperatures (SSTs) in the Pacific equatorial cold tongue (ECT) are a longstanding bias in coupled general circulation models (CGCMs) (Mechoso et al. 1995; de Szoeke and Xie 2008; Zheng et al. 2012; Li and Xie 2014). This ECT SST bias has pronounced impacts on the climate of the tropical Pacific and the globe in general (de Szoeke and Xie 2008; Zuidema et al. 2016), degrading predictions of ENSO and its remote impacts (Wittenberg et al. 2006; Watanabe and Wittenberg 2012; Xue et al. 2013; Vannière et al. 2013; Xue et al. 2013; Vecchi et al. 2014; Guilyardi et al. 2016). In CGCMs the ECT tends to be too intense and extend too far west, inhibiting rainfall in the western equatorial Pacific (Zheng et al. 2012) and generating excessive easterly trade

winds and an overly steep slope of the thermocline along the equator. ECT SST biases also play a role in models' insufficient cross-equatorial asymmetry of rainfall, winds, and thermocline depth, and in their stronger-than-observed semiannual cycle of equatorial SSTs in the east Pacific (Chang 1996; Wang and Wang 1999).

Climatological ECT biases in simulations further affect the spatial distribution of warm SST anomalies (SSTAs) during El Niño, displacing the SSTA patterns westward in coupled GCMs and affecting the balance of coupled feedbacks (Ham and Kug 2012; Kug et al. 2012; Capotondi et al. 2015; Graham et al. 2017). The cold tongue bias also affects the simulated sensitivity of ENSO to natural and anthropogenic climate forcings (Power et al. 2013; Cai et al. 2014).

Attribution of ECT biases is complicated by the relatively short record of instrumental observations of tropical Pacific climate, combined with the strong air–sea

coupling of the Pacific climate system and the pronounced low-frequency climate variations arising from volcanic eruptions, anthropogenic forcings, and intrinsic chaos (Wittenberg 2015; Capotondi et al. 2015). The causes of ECT biases are also model dependent (Zuidema et al. 2016). Li and Xie (2014) highlight the role of excessive easterly winds in the western Pacific in shoaling the thermocline in the eastern equatorial Pacific, which amplifies ECT cold biases via the zonally oriented Bjerknes feedback. Others have highlighted the roles of the following: overly strong or deep equatorial upwelling (Zheng et al. 2012) and vertical mixing (Jia et al. 2015); an equatorial thermocline that is too shallow or too deep (Li and Xie 2012); excessive evaporation or cloud shading (Burls and Fedorov 2014; Dai 2006); sunlight penetrating to the wrong depth, either on- or off-equator (Anderson et al. 2007); and insufficient lateral stirring from tropical instability waves (TIWs; Jochum et al. 2007). Advection by eddies within the mixed layer (ML; Swenson and Hansen 1999) and vertical mixing due to TIWs (Moum et al. 2009, 2013; Inoue et al. 2012), especially near the thermocline (Liu et al. 2016), have also been posited as affecting the intensity of the ECT.

Part I (Ray et al. 2018, hereafter Part I) of this two-part paper introduced a diagnostic framework to summarize the oceanic contributors to the climatological ECT intensity. In Part II, we use the framework to assess the ECT temperature budget of the GFDL-FLOR global coupled GCM, with reference to observations and ocean reanalyses. We further examine a flux-adjusted (FA) simulation of FLOR with a corrected climatology of SST and surface wind stress, which helps to distinguish between the initial seeds of bias in the individual model components, and the amplifiers and modifiers of that bias when the ocean and atmosphere are coupled. We conclude with a discussion of the implications of our results for the proposed redesign of the Tropical Pacific Observing System (TPOS2020; Cravatte et al. 2016) and for phase 6 of the Coupled Model Intercomparison Project (CMIP6; Eyring et al. 2016).

2. Datasets

a. Observations and reanalyses

As described in Part I, for surface observations we use SST from HadISST.v1 (Rayner et al. 2003), surface heat fluxes from TropFlux.v1 (Praveen Kumar et al. 2012), and surface wind stress from ERA-Interim (Dee et al. 2011). Subsurface temperature and currents are from SODA 2.2.4 (Giese and Ray 2011), ORA-S4 (Balmaseda et al. 2013), and the GFDL Ensemble Coupled Data Assimilation (ECDA) v3.1 (Chang et al. 2013) ocean reanalyses. Except where otherwise noted, all observations and reanalyses products used for this study span the period 1980–2010. To examine TIW activity we also use the NOAA OISST.v2

high-resolution daily dataset (Banzon et al. 2016) from 1982–2010. See Part I for further details.

b. FLOR coupled GCM

Vecchi et al. (2014) describe the formulation of the FLOR global coupled GCM (the forecast-oriented low ocean resolution version of CM2.5), and Wittenberg et al. (2018) describe its simulation of the tropical Pacific climatology. Part I provides further details on the FLOR simulations used in this study.

c. Flux-adjusted coupled GCM (FLOR-FA)

To examine the impacts of FLOR's remaining surface biases (Fig. 1a) on its tropical Pacific subsurface climatology and heat budget, we further examine a 30-yr (years 21–50) flux-adjusted version named FLOR-FA. FLOR-FA is identical to FLOR, except that it has "flux adjustment" (FA) applied to its surface wind stress, heat flux, and freshwater flux to maintain the surface climatology close to observations, without restricting the development of anomalies about the climatology (Wittenberg et al. 2018, unpublished manuscript). The FA is spatially and seasonally varying, but does not change from year to year. By design the FA substantially reduces the simulated mean SST and wind stress biases (Fig. 1b), although a warm SST bias remains near South America and along 5°–10°N in the central Pacific.

3. Budget framework

a. Volume-mean temperature tendency

As described in Part I, given a *stationary* three-dimensional domain D with volume V_D and volume-mean temperature T_D, the time tendency of T_D is given by

$$\partial_t T_D = \frac{Q_{\text{sfc}} - Q_{\text{pen}}}{\rho_0 C_p V_D} + \langle \text{advection} \rangle + \langle \text{vertical mixing} \rangle + \langle \text{other} \rangle, \quad (1)$$

where ∂_i indicates a partial derivative in the i direction, $\langle \rangle$ denotes a volume average over D, $T_D = \langle T \rangle$, $\rho_0 = 1035 \text{ kg m}^{-3}$ is a constant seawater reference potential density, $C_p \approx 3992 \text{ J kg}^{-1} \text{ K}^{-1}$ is the specific heat capacity of seawater, Q_{sfc} is the (positive downward) horizontally averaged net surface heat flux, and Q_{pen} is the (positive downward) horizontally averaged penetrative solar flux at the base of D. Because of the stationary domain, there is no detrainment tendency. "Other" denotes additional processes (e.g., subgrid-scale lateral mixing, nonlocal vertical mixing, sub-mesoscale mixing, and sensible heating due to rainfall and rivers) that in the ocean model play a relatively minor role in the temperature budget of the tropical

Mean SST and wind stress biases
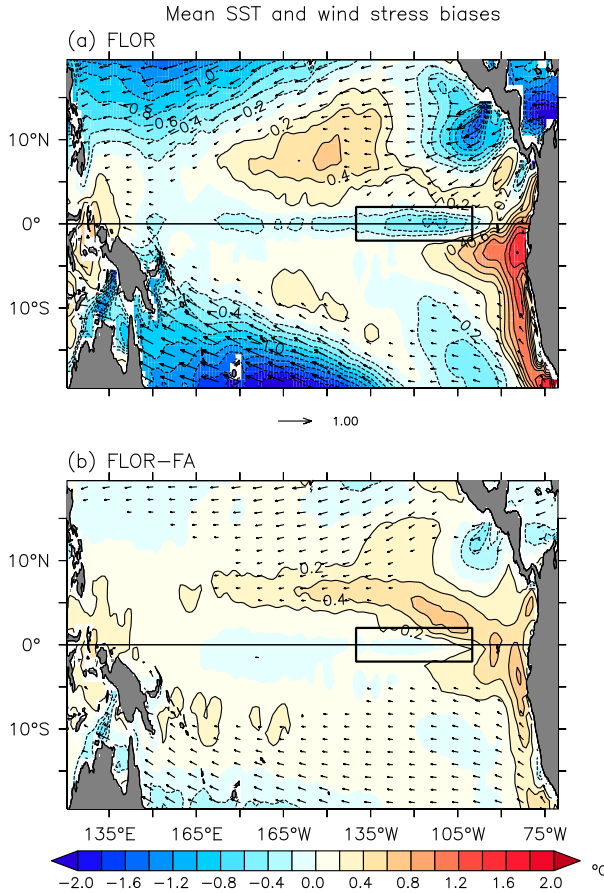
(a) FLOR

(b) FLOR−FA

FIG. 1. Climatological annual mean SST biases (shading) from 100-yr FLOR control simulations, relative to HadISST observations (1981–2010), in (a) FLOR, and (b) flux-adjusted FLOR (FLOR-FA). Vectors indicate surface wind stress biases (dPa) relative to ERA-Interim (1981–2010), with westward vectors indicating westward stress on the ocean. Only wind stress biases exceeding 0.1 dPa are shown. The black box indicates the ECT region (2°S–2°N, 140°–100°W).

Pacific upper-ocean domains that we examine here. The resolved advective tendency is

$$\langle \text{advection} \rangle = -\frac{1}{V_D} \int_{S_D} (\mathbf{u} \cdot \mathbf{n})(T - T_D)\, dS, \qquad (2)$$

where S_D is the bounding surface of D, $\mathbf{u} = (u, v, w)$ is the three-dimensional current velocity, $\mathbf{n}$ is the outward unit normal vector along S_D, T is temperature, and $T - T_D$ is the temperature anomaly at the boundary relative to the domain average. The local component of parameterized subgrid-scale vertical mixing is

$$\langle \text{vertical mixing} \rangle = \langle \partial_z (\kappa_z \partial_z T) \rangle$$
$$= -\frac{1}{V_D} \iint_{S_{-h}} \kappa_z \partial_z T\, dx\, dy, \qquad (3)$$

where z is upward, κ_z is the local instantaneous vertical diffusivity, and $\iint_{S_{-h}}$ denotes integration along the layer base.

b. Layer definitions

As in Part I, we define h as the depth at which the potential density referenced to the surface σ reaches a critical difference $\Delta\sigma_{\text{crit}}$ from the local surface value $\sigma(z = 0)$. We denote a particular choice of h using this shorthand: $H_{\Delta\sigma_{\text{crit}}\tau}$. The subscript letter τ indicates the time averaging method applied to the T and S fields, before computing σ and h. Part I examined various averaging methods for τ, including hourly ("h"), daily ("d"), monthly ("m"), climatological monthly ("c"), stationary climatological annual ("a"), or fixed depth ("f").

Here we draw on the results of Part I, and focus only on two stationary, nested layers. For the surface mixed layer (SML) whose temperature is highly correlated with SST, we use $H_{0.3a}$, denoting a criterion of $\Delta\sigma_{\text{crit}} = 0.3\,\text{kg}\,\text{m}^{-3}$ applied to the three-dimensional climatological annual mean T and S. For the thicker advective layer (AL) that subsumes nearly all of the local diffusive heat fluxes from vertical mixing, we use $H_{1.4a}$, denoting a criterion of $\Delta\sigma_{\text{crit}} = 1.4\,\text{kg}\,\text{m}^{-3}$ applied to the climatological annual mean T and S. The part of the AL that lies below the SML, where heat diffusing down from the SML converges and is balanced mainly by monthly advective cooling, is referred to as the advective–diffusive layer (ADL). Figure 5 of Part I, and appendix A of this paper, show the resulting layers for FLOR, FLOR-FA, and SODA, and their relation to the SST and vertical diffusive heating.

c. Equatorial vertical structure: FLOR versus SODA

Figure 2 shows differences between the time-mean monthly-scale advection components computed from FLOR and SODA. Unlike FLOR (which was shown in Fig. 12 of Part I), SODA produces localized spikes along the equator, particularly for the vertical advection. These spikes arise from imperfect assimilation of the zonally sparse TAO mooring data into the SODA ocean model, which results in spurious persistent upwelling features near the moorings. Appendixes B and C discuss these features, and describe the large differences in equatorial currents and advective terms diagnosed from the SODA, ORA-S4, and ECDA.v3.1 reanalyses, which highlight a continuing need for improved observations and reanalyses to better constrain simulations of the equatorial Pacific. Thus in what follows, the heat budget comparisons between FLOR and SODA (particularly for the vertical component) should be taken as indicative of possible model biases, though not definitive.
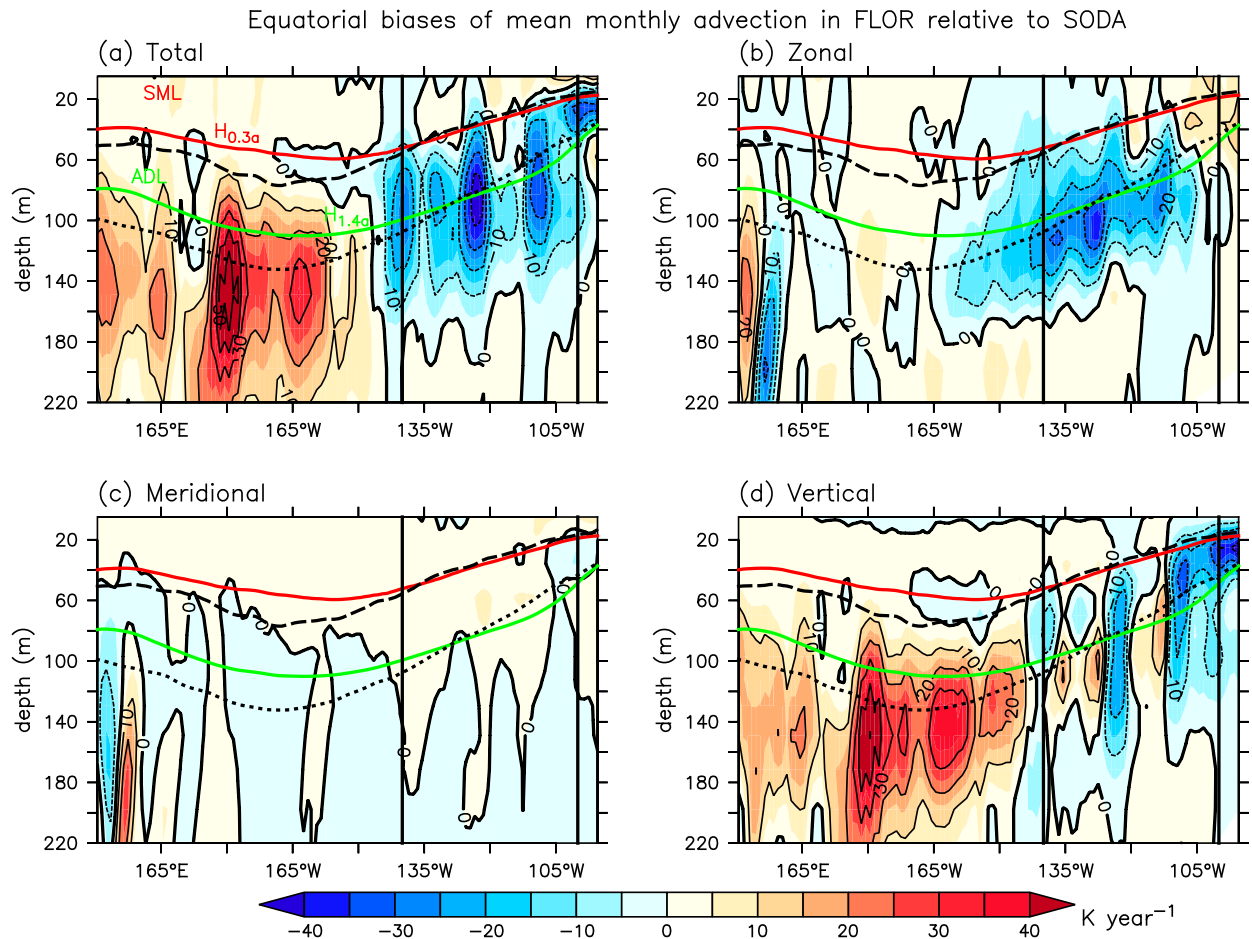
FIG. 2. Equatorial sections of the difference in time-mean monthly-scale advection, for the FLOR simulation minus the SODA v2.2.4 reanalysis (1980–2010): (a) total, (b) zonal, (c) meridional, and (d) vertical. Shading is incremented every half contour. Solid curves indicate the depths of the SML ($H_{0.3a}$; red) and AL ($H_{1.4a}$; green) in FLOR. $H_{0.3a}$ (black dashed curve) and $H_{1.4a}$ (black dotted curve) diagnosed from SODA v2.2.4 are plotted for comparison with that from FLOR. Vertical lines indicate the boundaries of the ECT.

FLOR's $H_{0.3a}$ is about 10–20 m shallower than SODA's to the west of the ECT, but within the ECT FLOR's $H_{0.3a}$ is very similar to SODA's. This suggests that any differences between the budgets of FLOR and SODA would need to stem from structural differences in the temperatures, currents, and budget terms within the SML, rather from differences in the SML depth itself. Figure 2 also shows the equatorial structure of the time-mean biases in the monthly advective components in FLOR relative to SODA 2.2.4. In the ECT region (2°S–2°N, 140°–100°W), FLOR shows stronger total monthly advective cooling than SODA, both within and below the ADL. FLOR's stronger cooling is due to both weaker zonal advective export of cold water across the sloping ADL base [due to FLOR's flatter equatorial thermocline and weaker Equatorial Undercurrent (EUC) in the ECT], and stronger vertical advective cooling (especially in the eastern part of the ECT, due to FLOR's stronger upwelling there).

FLOR's stronger monthly advective cooling of the ECT ADL suggests that it may be balanced by a stronger diffusive heat transfer from the SML to the ADL than in SODA—perhaps linked to FLOR's weak TIWs, which could contribute to reduced equatorial stratification and increased vertical mixing. West of the ECT, FLOR shows weaker monthly vertical advective cooling than SODA in and below the ADL; this is associated with both FLOR's flatter equatorial thermocline (which weakens $\partial_z \overline{T}$ below 125-m depth in the west Pacific) and FLOR's weaker upwelling in the western equatorial Pacific relative to SODA.

4. Spatiotemporal structure of the layer temperature budgets

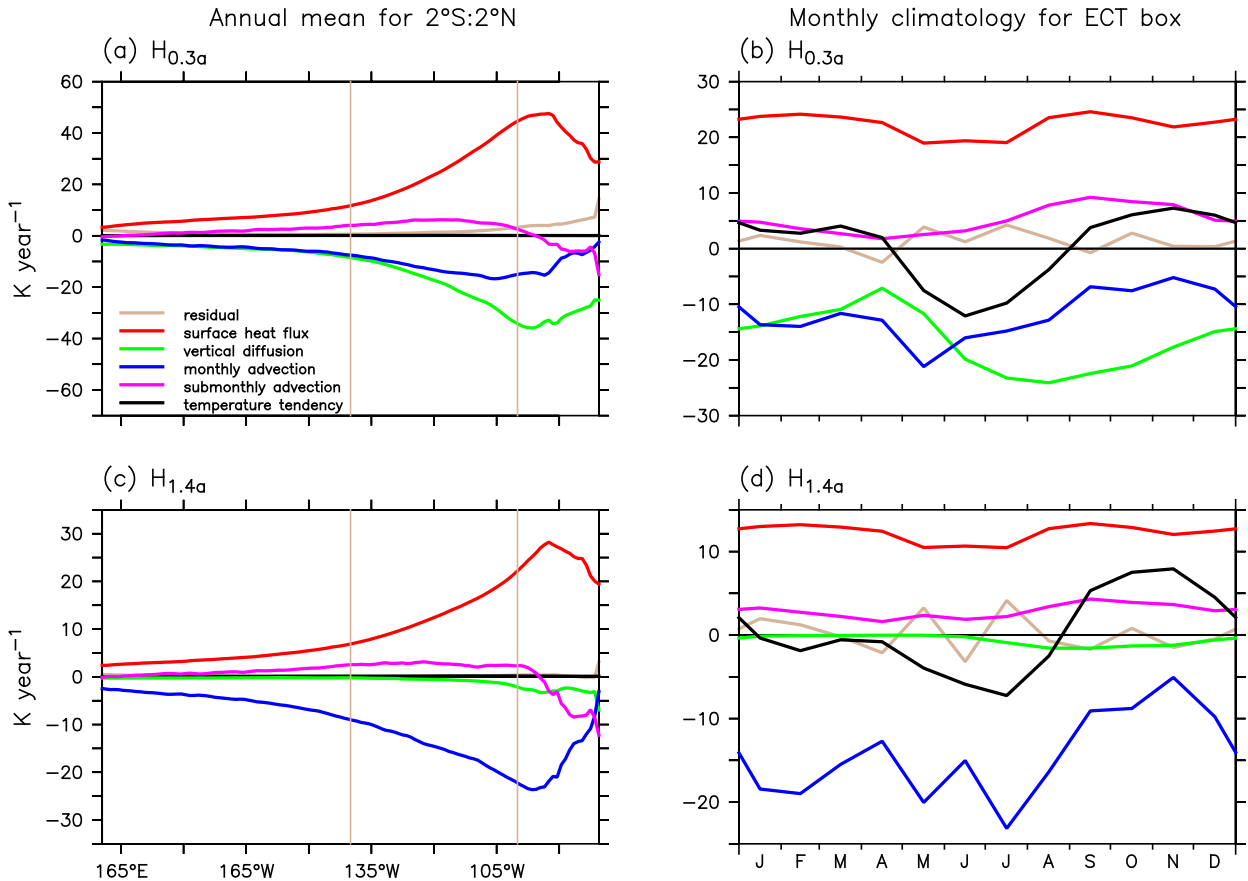To provide spatiotemporal context for the annual-mean temperature budget of the ECT, this section describes

FIG. 3. FLOR-simulated layer temperature budgets for (left) the 2°S–2°N band as a climatological annual mean, and (right) the ECT box as a 12-month climatology. The budget extends vertically over (a),(b) the SML ($H_{0.3a}$) and (c),(d) the AL ($H_{1.4a}$). Colors indicate the net surface heat flux minus shortwave penetrating through the layer base (red), parameterized local diffusion due to vertical mixing (green), monthly advection (blue), all submonthly advection including subdaily advection (magenta), and the sum of all remaining terms (gray). Vertical lines in (a) and (c) show the zonal extent of the ECT box.

the locations, seasons, and ENSO phases where each of the tendency terms is particularly active in FLOR. The present study is focused mainly on evaluating the time-mean heat budget of the ECT in FLOR; evaluation of the spatiotemporal evolution of the budget relative to observational reanalyses will be presented in future work.

a. Zonal structure along the equator

Figure 3a summarizes the zonal structure of FLOR's annual-mean SML temperature budget along the equator. For each month and for each grid cell along the zonal direction, the budget of (1) is evaluated for a yz-oriented volume extending from 2°S to 2°N and from the surface to $H_{0.3a}$. The time means of these budgets are then displayed in Fig. 3a. The SML budget terms are stronger toward the eastern side of the ECT box, where the shallower thermocline enhances the vertical heat transport by oceanic advection and mixing, cooler SSTs weaken evaporative

cooling, and reduced cloudiness enhances the shortwave heating of the ocean. The surface flux heating peaks near 95°W and is balanced primarily by vertical diffusive cooling, which peaks at nearly the same longitude, and monthly (mainly vertical) advective cooling, which peaks near 105°W. East of the ECT the easterly trade winds and associated upwelling weaken, so that the total monthly advective cooling becomes weaker than the vertical diffusive cooling along the equator. West of the ECT, the deeper thermocline attenuates both the monthly advective cooling and diffusive cooling, but the relative importance of the monthly advective cooling grows due to the stronger upwelling maintained by the stronger easterly trade winds west of the ECT. Submonthly (mainly meridional) advection is a weak warming term in and west of the ECT where the simulated TIWs are most active, and peaks near 115°W; on the other hand, the submonthly (mainly subdaily) advection is a cooling term

east of the ECT, where the shallower thermocline enhances the SML cooling effect of transient vertical mixing. The sum of the remaining terms (gray residual line) is weak and plays little role in the SML annual-mean budget.

Figure 3c shows the temperature budget for the full AL. Note that $H_{1.4a}$ is sufficiently deep that there is little vertical diffusive flux out of the volume, so that vertical diffusion plays little role in the budget for AL-averaged temperature. Monthly (mainly vertical) advective cooling almost completely balances the surface flux heating, except in the shallower-thermocline region east of the ECT where there are also cooling contributions from submonthly advection and vertical diffusion. In the ECT region, submonthly (mainly meridional) advection acts to warm the AL, although this effect (mainly associated with TIWs) is weak compared to the surface heat fluxes.

b. Seasonal cycle

Figure 3b shows the climatological seasonal cycle of FLOR's SML temperature budget terms for the ECT box. For each month, the volume-mean budget of (1) is evaluated for the ECT box spanning 2°S–2°N, 140°–100°W, from the surface to $H_{0.3a}$, and the 12-month climatology of this budget is then displayed in Fig. 3b. All of the individual climatological budget terms retain their qualitative roles (i.e., they keep the same sign) throughout the year, in contrast to the total SML tendency (black line) which shows intense cooling in May–June (MJJ) followed by gradual warming the rest of the year. The SML temperature variations are *not* driven mainly by surface fluxes, which provide relatively uniform net heating throughout the year and have only weak semiannual February/September peaks and June/November minima (associated mainly with the seasonal variations in solar zenith angle near the equator). Rather, the intense MJJ cooling of the ECT SML is driven mainly by strengthening vertical diffusive cooling in MJJ (associated with the shallower thermocline and stronger near-surface thermal stratification in that season), which is later countered in August–October (ASO) by weakening monthly advective cooling (as the thermocline deepens) and strengthening submonthly heating (as the TIWs become more active).

The seasonal progression of ECT SML budget is as follows. Strong monthly advective cooling in April–June (AMJ), followed by weak surface flux heating (MJJ) and strong vertical diffusive cooling [July–September (JAS)], leads to rapid total cooling in MJJ as described above. This MJJ cooling is then followed by strong surface flux heating (ASO, when solar zenith angle is greatest) and submonthly advective warming (August–November, when TIWs and $\partial_y \overline{T}$ are jointly strong), terminating the ECT

cooling season. Next the monthly advective cooling weakens (September–December, when the thermocline is seasonally deeper), leading to gradual net warming during September–April as the vertical diffusive cooling gradually weakens [March–May (MAM), when ECT wind speeds and TIWs slacken, reducing the shears and kinetic energy available for mixing]; this is somewhat opposed by weakened submonthly advective warming (MAM, when TIWs are weak). The monthly advective cooling strengthens again in AMJ as the thermocline shoals, terminating the ECT warming season.

Figure 3d shows the seasonal cycle of FLOR's ECT AL temperature budget. In a similar manner as for the SML, the AL climatological terms retain their qualitative roles (keeping the same sign) throughout the year. The total AL tendency shows strong cooling during MJJ (as did the SML tendency), but also strong warming during September–December. The seasonal cycle of AL temperature is driven mostly by monthly (mainly vertical) advective cooling associated with seasonal variations in thermocline depth, with vertical diffusion playing almost no role. The monthly advective cooling is weakest during September–November, due mainly to a relaxed $\partial_z \overline{T}$ associated with a seasonally deepened thermocline.

c. ENSO composites

Figure 4 shows a composite of FLOR's ECT temperature budget for the SML ($H_{0.3a}$), averaged over all eight El Niño events and nine La Niña events occurring during the 30-yr FLOR simulation. As was the case with the seasonal cycle, the budget terms again generally maintain their qualitative roles throughout these interannual events, without changing sign. The sole exception is the monthly zonal advection (Figs. 4d,j), which cools the SML most of the year but warms it in AMJ (due to the seasonal weakening of the equatorial easterly trade winds, which weakens the westward SEC and strengthens the eastward EUC).

At the onset of El Niño (Figs. 4a–f) there is an anomalous net warming of the ECT SML (Fig. 4b; black solid minus black dashed), due to weakening of the usual seasonal monthly-scale vertical and meridional advective cooling during April–July(0). This anomalous warming is driven by a rapidly deepening thermocline in the eastern equatorial Pacific, which warms the water entrained into the equatorial SML; this warmer water is then spread poleward by the background Ekman-driven poleward currents within the SML. The parameterized vertical diffusive cooling, which as we have shown is critical to the SML in both the annual-mean budget (Fig. 3a) and seasonal cycle (Fig. 3b), initially does not deviate from its typical seasonal cycle and thus does not contribute to the initial anomalous warming.
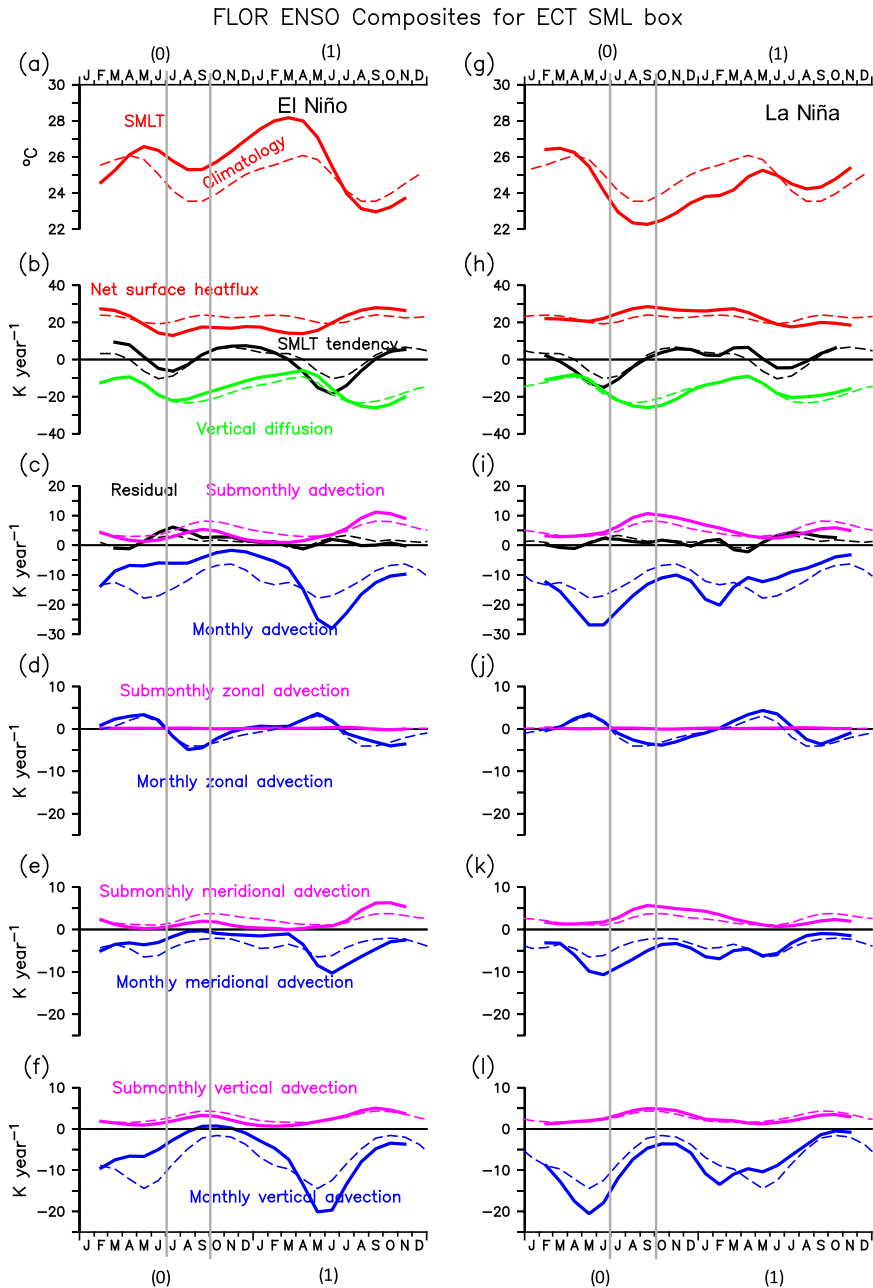
FIG. 4. Time evolution of (left) El Niño and (right) La Niña composite temperature tendency terms (K yr^{-1}) for the ECT SML box ($H_{0.3a}$), averaged over the 30-yr FLOR simulation. Total (solid) and climatological (dashed) values are shown; their difference defines the anomaly. Shown are (a),(g) SML temperature (red; °C); (b),(h) SML temperature tendency (black), net surface heat flux minus penetrative shortwave (red), and local diffusion due to vertical mixing (green); (c),(i) monthly advection (blue), submonthly advection (magenta; not including subdaily), and residual sum of all remaining terms (black). The remaining panels decompose the monthly advection (blue) and submonthly advection (magenta) into (d),(j) zonal, (e),(k) meridional, and (f),(l) vertical components. Gray vertical lines highlight the JAS season of strong TIW activity.

Partially opposing the anomalous warming are both a weaker surface flux heating (due to enhanced evaporative cooling associated with the anomalously warm SSTs, and greater shading of the surface by deep convective clouds) and weaker submonthly advective heating (associated both with weakened meridional current shears and TIW stirring near the ECT, and with weakened $\partial_y T$ and $\partial_z T$, which reduce the heat transport by submonthly stirring). With the weakened monthly advective cooling (and unchanged vertical diffusion) no longer fully balancing the heating from the net surface fluxes and submonthly stirring, the SML begins to warm.

The El Niño peaks as the thermocline shoals and the monthly vertical advective cooling in the ECT is re-established near the end of the calendar year. The net cooling accelerates until May(1), due to stronger monthly vertical and meridional advective cooling (associated with both the shoaling thermocline and the gradually strengthening equatorial westward SST gradient, easterly trade winds, and monthly-scale upwelling in the ECT) and weaker warming from both surface fluxes (due to increased evaporation and cloud shading) and submonthly meridional advection (due to weakened TIW stirring and weakened $\partial_y T$). The weakened vertical diffusive cooling is the last of the terms to (slightly) oppose the demise of El Niño. By the time El Niño ends in July(1), the monthly advective cooling is anomalously strong due to the anomalously shallow equatorial thermocline, inducing subsequent anomalous cooling of the SML. The strongest SML $\partial_t T$ events in the FLOR simulation occur during the intense vertical advective cooling after the peak of El Niño, which frequently initiates an overshoot into La Niña (see Part I; Fig. 3c).

At the onset of La Niña (Figs. 4g–l) there is an anomalous cooling of the ECT SML, due to an enhancement of the usual seasonal monthly-scale vertical and meridional advective cooling during March–July(0). As described above this cooling is mainly driven by an anomalous shoaling of the east Pacific thermocline, often following an El Niño event. As was the case for El Niño, the parameterized vertical diffusion hardly contributes to the La Niña anomalous cooling. The submonthly advection also does not contribute to the initial cooling.

By the peak of La Niña in February(1), the anomalous monthly advective cooling has weakened due to a gradual deepening of the ECT thermocline and warming of the waters entrained into the SML. In addition, there is enhanced warming from surface fluxes (due to reduced cloudiness and evaporation, associated with the anomalously cold SSTs) and submonthly meridional advection (due both to intensified meridional current shears and TIW stirring near the ECT and to enhanced $\partial_y T$ and $\partial_z T$,

which strengthen the heat transport by submonthly stirring). The La Niña then decays as the thermocline continues to deepen and the anomalous monthly advective cooling weakens, allowing the enhanced warming from surface fluxes and submonthly advection to dominate the SML temperature tendency. By the time the cold event ends in June(1), the thermocline is anomalously deep and the monthly (mainly vertical) advective cooling is anomalously weak, inducing subsequent anomalous warming of the ECT SML, despite the gradually weakening heating from surface fluxes and submonthly advection.

The ECT SML advective terms are thus strongly affected by ENSO in FLOR. The monthly vertical advective cooling (which in the ECT is mostly controlled by the variations in thermocline depth) is strongest during March(0) of La Niña years, and vanishes during October(0) of El Niño years. The submonthly advective warming (controlled mainly by the level of TIW activity and the background intensity of $\partial_y T$ and $\partial_z T$) are strongest during September(0) of La Niña, and vanish during March(1) of El Niño. Monthly zonal advection contributes relatively little to the interannual variability within the ECT; however, it is important west of the ECT, where the zonal SST gradient is stronger. Submonthly zonal advection contributes hardly at all to the interannual temperature variations of the ECT; its main role is simply to take the relatively warm water brought into the ECT by submonthly meridional advection and redistribute it westward within the ECT.

In FLOR the vertical diffusive cooling of the ECT SML is relatively unaffected by ENSO. Even when the thermocline is at its deepest, during MAM at the peak of El Niño, vertical diffusion continues to act as a substantial cooling term for the SML, offsetting most of the heating from surface heat fluxes. By countering much of the damping of ENSO by surface fluxes and submonthly advection, the interannual variations in vertical diffusive cooling permit the SSTs to be governed more strongly by the monthly advective terms.

5. Correcting the surface climatology via flux adjustments

To help isolate the impacts of surface biases on the ECT temperature budget, we next examine FLOR-FA, the flux-adjusted version of FLOR. Figure 1 shows that the FA largely removes FLOR's cold biases in the ECT and in the southwest and northwest tropical Pacific and weakens FLOR's excessive tropical Pacific easterly wind stress away from the equator. Wittenberg et al. (2018, unpublished manuscript) shows that this greatly reduces FLOR's excessive wind stress cyclonicity, Ekman suction,

and poleward Sverdrup transport over the tropical Pacific region, which helps to deepen the equatorial thermocline. Puzzlingly, the FA has an adverse effect on the equatorial subsurface thermal structure, overly deepening the equatorial thermocline and SML (Fig. 6, red and green lines). Relative to FLOR, FLOR-FA's SML deepens by more than 10 m in the ECT and 40 m near 170°W.

Figure 5 shows the change in the equatorial SML temperature budget due to the flux adjustments. The largest changes are in the eastern equatorial Pacific, where the thermocline is shallow and the SML budget terms are strong (Fig. 3a). Despite FLOR's cold SST bias in the ECT region (Fig. 1), the FA actually *weakens* the surface flux heating of the ECT. This counterintuitive result stems from the wind stress adjustments mentioned above, which deepen the equatorial thermocline and SML and weaken the ability of the ECT to take up heat from the atmosphere. Consistent with FLOR-FA's warmer equator being driven by subsurface changes, FLOR-FA shows weaker ECT cooling from both monthly advection (especially in the east near 1°N) and vertical diffusion (mainly on the equator). FLOR-FA's warmer SML is slightly tempered by weaker submonthly advective warming of the ECT SML.

Figure 6 shows the equatorial vertical structure of the subsurface changes induced by the FA. The upper-ocean warming in FLOR-FA relative to FLOR is induced mainly by weaker monthly vertical advective cooling (due to weaker $\partial_z \overline{T}$), which dominates over the weaker monthly zonal advective warming (due to a weaker and deeper EUC). The net result deepens and weakens the net monthly advective cooling of the AL, which destratifies and deepens the SML along the equator, and steepens the zonal slope of $H_{0.3a}$ within the ECT. Changes in monthly meridional advection play little role at the equator, although they do contribute some slight additional warming in FLOR-FA above 40 m east of 120°W.

Thus despite improving the surface fields, the FA seemingly *degrades* aspects of the subsurface simulation in FLOR relative to SODA. The fact that the ECT SML is too deep in FLOR-FA—despite corrected SST and surface wind stress—suggests that there are biases in the ocean model's equatorial temperature budget, which are obscured in the unadjusted FLOR by excessive off-equatorial cyclonic wind stress curl that helps to elevate the equatorial thermocline (Wittenberg et al. 2018). Since the advective cooling of the ECT ADL is almost entirely balanced by downward diffusion of heat from above, FLOR-FA's overly deep advective cooling suggests that it may also diffuse too much heat too far down into the water column. We explore the reasons for this in section 7a.
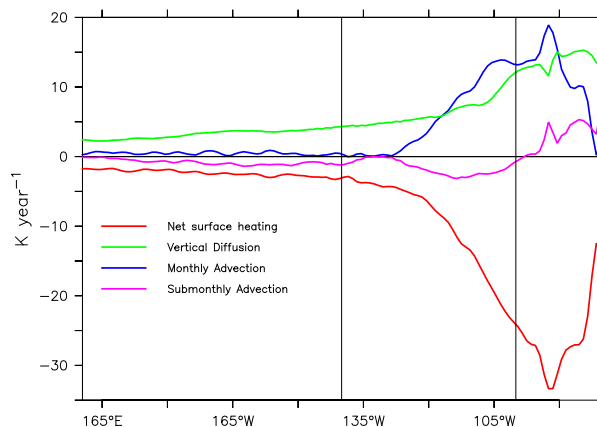

FIG. 5. Change in annual-mean SML temperature tendencies due to flux adjustment (FLOR-FA minus FLOR), for the equatorial band (2°S–2°N): net surface flux minus penetrative shortwave (red, includes the heat flux adjustment), local diffusion due to vertical mixing (green), monthly advection (blue), and submonthly advection (magenta, includes subdaily).

6. Evaluation of FLOR's annual-mean ECT temperature budget

a. FLOR versus SODA

1) USING EACH DATASET'S OWN LAYERS

Figure 7 decomposes the annual-mean ECT temperature budgets of SODA 2.2.4, FLOR, and FLOR-FA into their directional and temporal components. For the SML (Fig. 7a), FLOR's surface flux heating (term 1.1, red bar) is balanced primarily by cooling from vertical diffusion (term 1.3) and monthly meridional and vertical advection (terms 4.4 and 4.5); the monthly meridional cooling, which is mainly at the northern face of the ECT (term 4.1), is more than offset by submonthly meridional warming (term 5.4). Compared to SODA, FLOR shows somewhat weaker surface flux heating of its SML, with correspondingly weaker monthly meridional cooling at the north and south faces of the ECT (terms 4.1 and 4.2).

The SODA dataset unfortunately does not provide the submonthly advective and diffusive tendency terms, and so we estimate them here as a residual (term 3.1 in Fig. 7a). The SODA residual—which contains both the additional terms explicitly simulated by the SODA ocean model and the temperature corrections imparted by the data assimilation—represents about the same total cooling as FLOR's residual terms. At face value, SODA's budget would then suggest that FLOR's ECT SML takes up too little atmospheric heat mainly because FLOR's monthly meridional advective cooling (term 4.4) is too weak—and that any error in FLOR's submonthly advective heating (term 2.2) is compensated

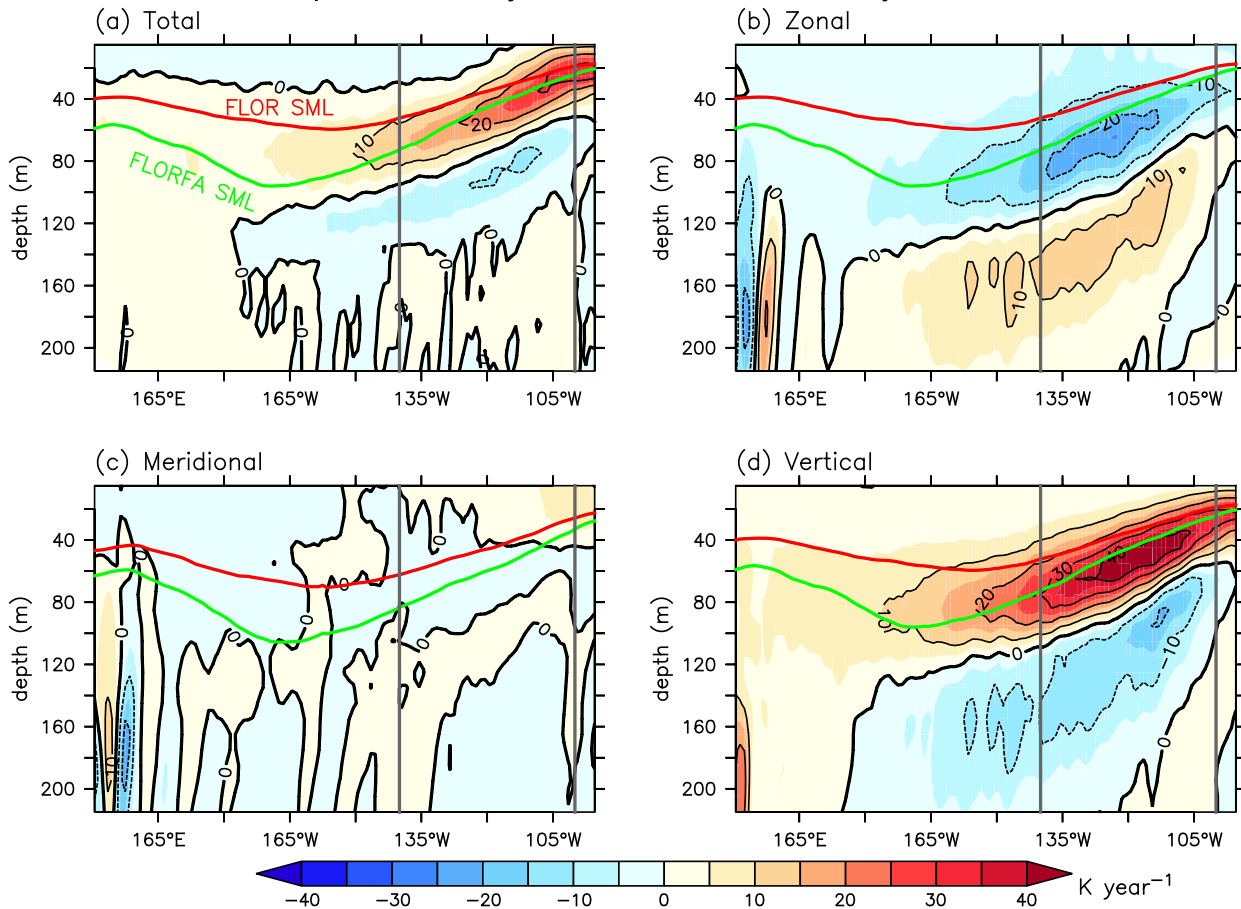## Impact of flux adjustments on mean monthly advection

FIG. 6. Equatorial sections of the change in mean monthly advective tendencies due to the flux adjustments (FLOR-FA minus FLOR): (a) total, (b) zonal, (c) meridional, and (d) vertical. Shading is incremented every half contour. The SML depth ($H_{0.3a}$; same in each panel) is indicated for FLOR (red line) and FLOR-FA (green line).

by an opposing error of equal magnitude in the vertical diffusive cooling (term 1.3) and/or other parameterized processes (term 1.5) affecting the SML.

For the full AL (Fig. 7b), FLOR's surface flux heating is balanced almost entirely by monthly advective cooling across the AL base and across the north and south faces of the ECT (terms 4.5 and 4.4), offset slightly by a weak submonthly advective warming across the northern and southern faces (term 5.4). Compared to SODA, FLOR has much stronger monthly advective cooling at the AL base (term 4.5), which is only partly offset by FLOR's weaker advective cooling across the north and south faces of the ECT (term 4.4).

FLOR's vertical diffusive cooling of the AL (term 1.3) is so weak that it offsets very little of the submonthly advective warming (term 2.2), leading to a net *warming* effect in its residual (term 3.1). In contrast, SODA shows a *cooling* effect from its residual. This suggests

several possibilities. First, FLOR's net submonthly advective warming of the AL (term 2.2) could be too strong, due either to excessive equatorward transport of off-equatorial heat (which seems unlikely due to FLOR's weak TIWs; Wittenberg et al. 2018) or to insufficient submonthly downward advection of heat. Second, FLOR's diffusive heat loss through the AL base (term 1.3) could be too weak, perhaps due to insufficient vertical mixing (e.g., due to FLOR's weak TIWs generating too little transient shear, particularly during boreal autumn and La Niña when $\partial_z T$ is especially strong). Third, SODA's residual cooling (term 3.1) may partly represent assimilation increments compensating for errors in the prescribed surface heat fluxes or simulated monthly advection (in turn possibly driven by wind forcing errors), such as a cooling correction to compensate for excessive surface heat flux, or for insufficient monthly advective cooling simulated by the SODA
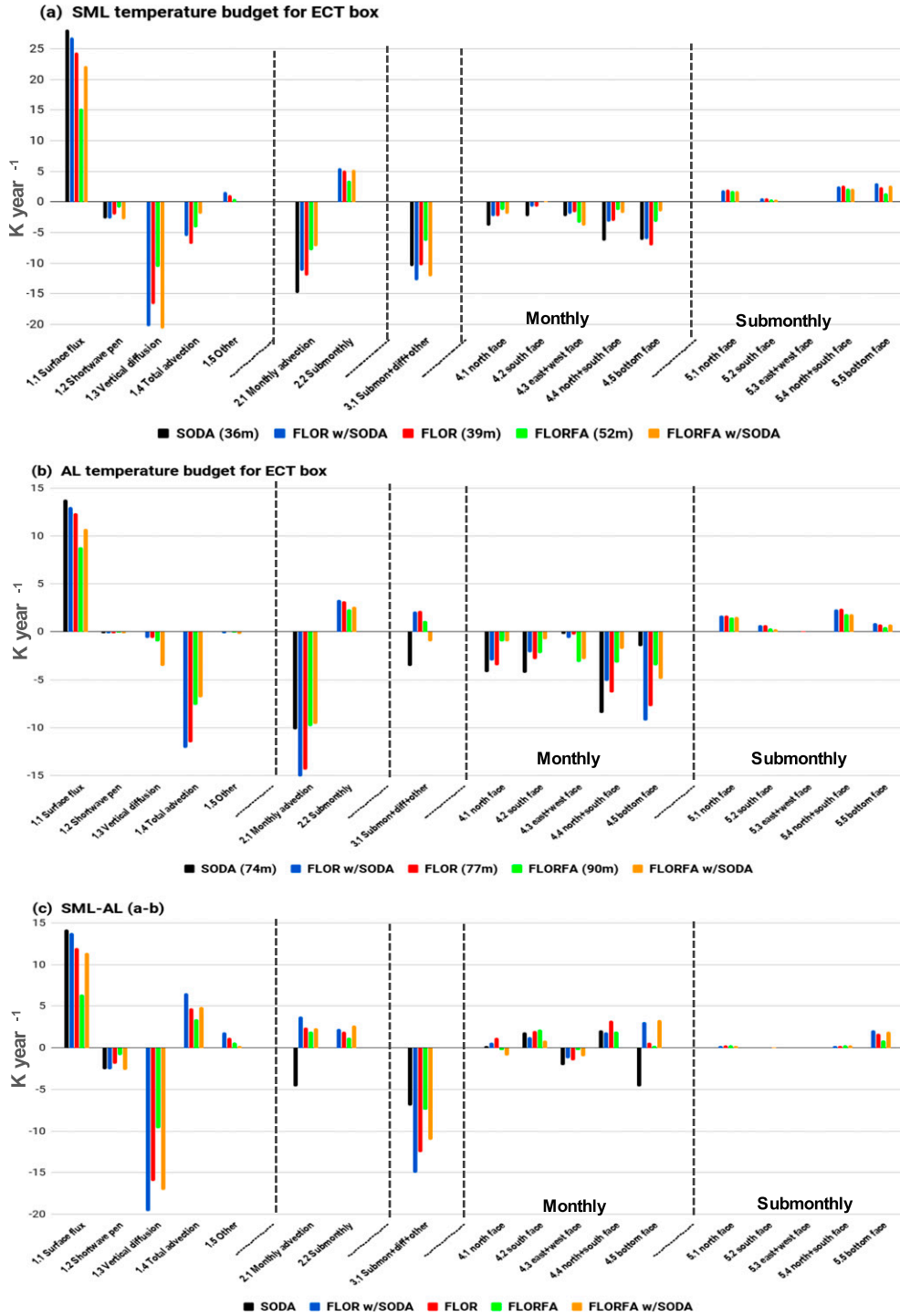
FIG. 7. Annual-mean ECT layer temperature tendencies ($K \, yr^{-1}$) for (a) the SML ($H_{0.3a}$), (b) the AL ($H_{1.4a}$), and (c) their difference [(a) − (b)]. Bar colors indicate different datasets: the SODA 2.2.4 reanalysis (1980–2010; black), FLOR simulation (30 yr) tendencies averaged over the SODA layers (blue) or FLOR layers (red), and the FLOR-FA simulation (30 yr) tendencies averaged over the FLOR-FA layers (green) or SODA layers (orange). Within each legend, the ECT-averaged layer thicknesses for each dataset are indicated in parentheses. For the surface heat flux (term number 1.1), the black bar indicates the TropFlux.v1 (1980–2010) fluxes converted to a temperature tendency using the SODA 2.2.4 layers. The "other" (term 1.5) denotes the residual tendency, 0 − (surface flux − shortwave penetration) − total advection − vertical diffusion. "Submonthly+diff+other" (term 3.1) denotes 0 − (surface flux − shortwave penetration) − monthly advection; for FLOR this is the total tendency arising from all submonthly processes including vertical diffusion, and for SODA it also includes any time-mean adjustments from the data assimilation.

model [perhaps due to its relatively flat EUC (Fig. B1a), which does weaken the total monthly advective cooling of the AL in SODA relative to the ORA-S4 and ECDA.v3.1 reanalyses (Figs. 2a, C1a, and C2a)].

It is not yet possible to winnow these possibilities, since none of the time-mean surface heat flux, the upwelling magnitude, or the diffusive heat fluxes in the ECT is yet well constrained by available observations or ocean reanalyses (see, e.g., appendixes B and C). Future observations relevant to the ECT heat budget, such as those proposed by the TPOS2020 project (Cravatte et al. 2016), could help to address this critical question.

2) CONTROLLING FOR DIFFERENCES IN LAYER THICKNESS

Some of the disparity between the SODA and FLOR temperature budgets stems from their differing layer thicknesses. The blue bars in Fig. 7 result from diagnosing FLOR's temperature budget only within the slightly thinner $H_{0.3a}$ layers from SODA, rather than from FLOR's own layers (red bars). For the SML (Fig. 7a), the blue bars are in closer agreement with SODA for the surface flux heating (term 1.1) and the monthly vertical and zonal advective cooling (terms 4.5 and 4.3). However, using SODA's shallower SML does not much change the monthly meridional advective cooling (term 4.4) diagnosed in FLOR. As a result, FLOR's total monthly advective cooling (term 2.1) is actually slightly weaker/worse when using SODA's shallower SML. FLOR does show more vertical diffusive cooling (term 1.3) when using SODA's shallower SML, so that the residual cooling (term 3.1) is now stronger than in SODA. This suggests that for the ECT volume spanned by SODA's SML, FLOR may overestimate the vertical diffusive cooling and/or underestimate the submonthly advective heating.

For the full AL (Fig. 7b), using SODA's slightly shallower $H_{1.4a}$ to diagnose FLOR's temperature budget similarly results in closer agreement of FLOR's surface heat flux term with SODA's. However, FLOR's monthly vertical advective terms (particularly the cooling from vertical advection, term 4.5) actually now show even *larger* discrepancies with SODA, when diagnosing these terms over the SODA AL.

3) INFLUENCE OF BUDGET TERMS ON THERMAL STRATIFICATION

Figure 7c shows the difference between the SML and AL terms in the ECT, namely the time-mean tendency of each term to stratify or destratify the AL by contributing to $\partial_t(T_{0.3a} - T_{1.4a})$. Positive terms in Fig. 7c are stratifiers, and negative terms are destratifiers. For both

SODA (black) and FLOR (red and blue), the upper ocean is *stratified* by the surface heat flux (term 1.1, which warms the SML more strongly than the AL as a whole) and by the monthly meridional advection (term 4.4, which cools the SML less strongly than the AL as a whole) act to *stratify* the upper ocean. Opposing this, the upper ocean is *destratified* by the summed submonthly and parameterized processes (term 3.1) and by monthly zonal advection (term 4.3), which both cool the SML more than the AL.

The role of monthly advection across the bottom of the SML and AL (term 4.5) differs strongly between SODA and FLOR: in SODA this term *destratifies* the water column by cooling the SML more than the AL, whereas in FLOR it *stratifies* the column by cooling the AL more than the SML. This difference in vertical advection is so strong that the *total* monthly advection (term 2.1) destratifies SODA but stratifies FLOR. This helps FLOR to maintain realistic stratification, despite FLOR's apparently excessive net destratification by summed submonthly and parameterized processes (term 3.1), associated with the SML being either excessively cooled by vertical diffusion or insufficiently warmed by submonthly advection, or the ADL being insufficiently cooled by submonthly advection.

Compared to SODA, FLOR's apparently stronger monthly advective cooling at depth (Fig. 7b, term 2.1) may thus be linked to excessive vertical diffusion and/or weaker TIWs in FLOR. Such biases could destratify the AL, deepening the thermocline and upwelling in FLOR until the monthly vertical advective stratifier becomes sufficiently intense to compensate.

b. Impact of flux adjustments

Compared to FLOR (red bars in Fig. 7), FLOR-FA (green bars) shows generally weaker layer-averaged temperature tendencies, since they are diluted by FLOR-FA's thicker layers. As discussed in Wittenberg et al. (2018, unpublished manuscript), FA weakens the excessive wind stress cyclonicity, Ekman suction, and poleward Sverdrup transport away from the equator, warming equatorial temperatures below 30-m depth and deepening the equatorial thermocline by 35 m.

Compared to FLOR, FLOR-FA greatly weakens the diffusion of heat from the SML into the ADL (term 1.3) and its destratifying effect on the AL (Fig. 7c). FA also strengthens the westward currents near the surface and their cooling effect on the ECT (term 4.3), weakening their destratifying effect as well. FLOR-FA has weaker $\partial_z \overline{T}$ above 100 m, which weakens the monthly vertical advective cooling (term 4.5) in both the SML and AL, but this does not much affect the stratifying tendency of that term (Fig. 7c).

Given that FLOR-FA has corrected climatological wind stress and SST, it is helpful to compare the ECT SML budgets between SODA (black bars in Fig. 7a) and the simulated terms evaluated over SODA's layers (FLOR in blue, FLOR-FA in orange). Compared to SODA and FLOR, for both the SML and AL, FLOR-FA simulates weaker net heating from surface fluxes (including the flux adjustment), weaker monthly meridional advective cooling (term 4.4), and stronger monthly zonal advective cooling (term 4.3). FLOR-FA also shows weaker monthly vertical advective cooling (term 4.5) of the SML than SODA and FLOR. For the AL, FLOR-FA shows weaker monthly vertical advective cooling than FLOR, though not as weak as SODA.

Evaluated over SODA's SML, FLOR-FA's residual cooling (term 3.1) is only slightly stronger than SODA's. Since FLOR-FA's TIW-induced submonthly warming of the SML is likely too weak (Wittenberg et al. 2018), it would seem that FLOR-FA may have too little vertical diffusive cooling of the SML (term 1.3), tied to FLOR-FA's overly deep thermocline and weakened $\partial_z \overline{T}$ near the surface.

Evaluated over SODA's AL, FLOR-FA's residual (term 3.1; orange bar) produces much less cooling than SODA (black bar). This is mostly compensated by FLOR-FA's weaker surface flux heating, so that FLOR-FA's net monthly advective cooling of the AL (term 2.1) actually closely resembles that in SODA. Yet compared to SODA, FLOR-FA shows a much weaker monthly meridional cooling (term 4.4), and stronger contributions from vertical and zonal advective cooling (terms 4.5 and 4.3). These biases are likely tied to FLOR-FA's stronger westward currents near the surface, and to FLOR-FA's deeper-than-observed thermocline—which both intensifies the thermal contrast across the base of the AL and weakens the thermal contrast between the warm poleward mean flow in the SML and the cold equatorward mean flow in the ADL.

Evaluated over the SODA AL, the total monthly advective cooling (term 2.1) weakens from FLOR (blue) to FLOR-FA (orange), due to FLOR-FA's weaker monthly vertical and meridional cooling (terms 4.5 and 4.4). This change is only partly offset by FLOR-FA's stronger vertical diffusive cooling (term 1.3) and monthly zonal advective cooling (term 4.3), with a slight additional contribution from weaker submonthly advective warming (term 2.2). Thus FLOR-FA is less able than FLOR to take up heat from the atmosphere (term 1.1).

Evaluated over the SODA AL, FLOR-FA has much *stronger* vertical diffusive cooling than FLOR, despite FLOR-FA's *weaker* $\partial_z \overline{T}$. This suggests that FLOR-FA's κ_z may be stronger than FLOR's at the AL base (indeed, this is confirmed by Fig. 10e). Although the real-world κ_z in the ECT is unknown, it may be that FLOR-FA's κ_z is too strong and extends too deep—due to either insufficient restratification by TIWs and/or a bias in the ocean model's κ_z formulation—and that this is the root cause of FLOR-FA's deep thermocline, despite its realistic climatological SSTs and wind stress forcing.

In the unadjusted FLOR, the thermocline-deepening effect of an excessive equatorial κ_z could be masked by too much off-equatorial Ekman suction and poleward Sverdrup transport (associated with the overly cyclonic off-equatorial wind stress), which could help to shoal the equatorial thermocline via excessive monthly vertical advective cooling below the SML (Fig. 7b, blue bar; term 4.5). This strong cooling of the ADL could then help FLOR to maintain strong AL stratification (Fig. 7c, blue bar; term 4.5), compensating the destratifying effect of excessive κ_z (Fig. 7c, blue bar; term 1.3).

FA strengthens the $\partial_y \overline{u}$ between the NECC and SEC in FLOR (Wittenberg et al. 2018, unpublished manuscript), which might be expected to strengthen FLOR's TIW activity. However, Fig. 7 shows that FA does *not* actually boost the submonthly equatorward heat transport in the SML and its stratifying effect on the AL; the reasons for this are discussed next.

7. Role of submonthly processes

a. Tropical instability waves

Satellite-based SST observations from the OISST.v2 high-resolution dataset (Banzon et al. 2016) show TIW-induced submonthly variations along the northern edge of the ECT box, mainly during August–November (Fig. 8a). These submonthly SST variations are underestimated in FLOR and FLOR-FA (Wittenberg et al. 2018), perhaps due to the ocean model's relatively coarse grid in the zonal direction (1°). Indeed the GFDL CM2.6 model (Delworth et al. 2012; Griffies et al. 2015), which has the same atmospheric component as FLOR but refines the ocean grid to 0.1°, shows greatly enhanced TIW activity and stronger submonthly advective warming of the ECT SML (Fig. 9). The ocean model formulation (e.g., the eddy viscosity parameterization) may also play a role; preliminary results from the MOM6 ocean component of the GFDL-SPEAR (Seamless System for Prediction and Earth System Research) coupled GCM show stronger TIW activity than FLOR, despite a horizontal ocean grid that is similar to FLOR's.

FLOR-FA shows weaker submonthly SST variations than FLOR (Fig. 8a), despite FLOR-FA's stronger $\partial_y \overline{u}$ between the NECC and SEC especially during July–September (Fig. 8b), and little change in the submonthly variance of the meridional currents near the
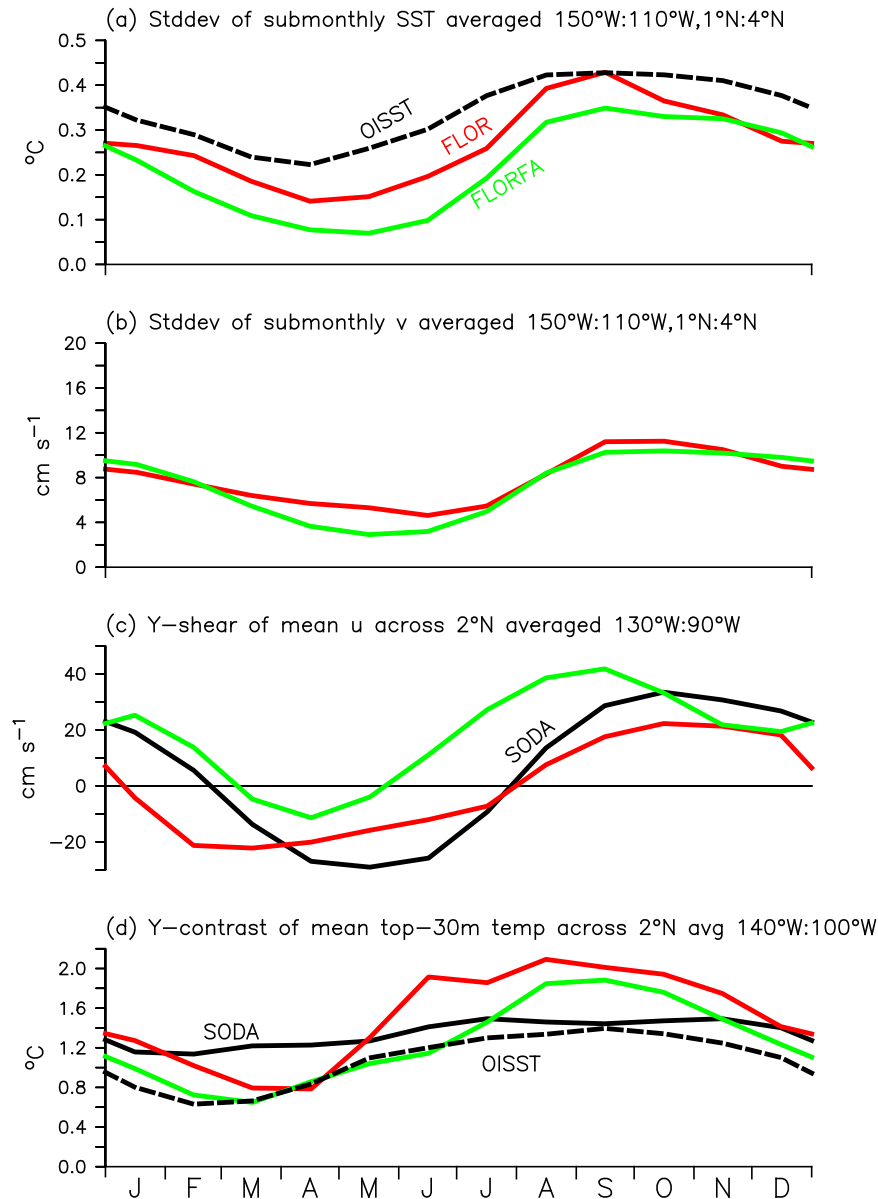
FIG. 8. Climatological seasonal cycle of near-equatorial fields relevant to Pacific TIW activity, for FLOR (red), FLOR-FA (green), SODA 2.2.4 (black solid; 1980–2010), and the OISST.v2 high-resolution daily dataset (black dashed; 1982–2010; Banzon et al. 2016). (a) Area mean (1°–4°N, 150°–110°W) of the standard deviation of submonthly SST (°C). The band-passed submonthly component is found by convolving the daily SST with a 41-day triangle kernel, subtracting that from the total SST, then convolving the result with an 11-day triangle kernel. (b) As in (a), but for the submonthly meridional currents (v; in cm), averaged over the top 30 m of the ocean before computing the standard deviation. (c) Climatological meridional shear of the zonal currents (u, in cm s^{-1}), computed as u (averaged over 2°–4°N) minus u (averaged over 0°–2°N), then averaged over 130°–90°W and over the top 30 m of the ocean. (d) Climatological meridional temperature gradient, computed as T (averaged over 2°–4°N) minus T (averaged over 0°–2°N), averaged over the top 30 m of the ocean and 140°–100°W.
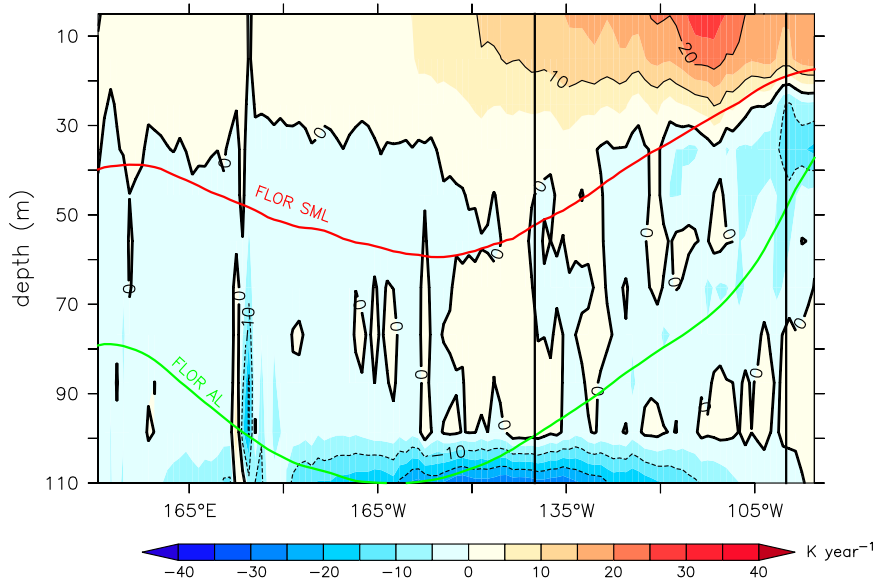
FIG. 9. Equatorial section of the submonthly advective heating *change* from FLOR (years 21–35) to CM2.6 (years 101–115). Shading is incremented every half contour. Solid curves indicate the depths of FLOR's SML ($H_{0.3a}$; red) and AL ($H_{1.4a}$; green).

ECT (Fig. 8b). This is partly because FLOR-FA's realistically weaker contrast between the equatorial and off-equatorial SST (Fig. 8d) serves to weaken the TIW *meridional* heat transports, while FLOR-FA's unrealistically deeper thermocline serves to weaken the TIW *vertical* heat transports.

TIWs are generated mainly north of the equator, due to meridional shear between the westerly North Equatorial Countercurrent (NECC) and easterly South Equatorial Current (SEC). The TIWs are most active between August and December, especially during La Niña events (Qiao and Weisberg 1995). TIWs stir cold ECT water poleward, where it absorbs heat from the atmosphere, and stir warm off-equatorial water into the ECT, weakening the ECT via meridional advective warming (Jochum et al. 2005; Menkes et al. 2006). TIWs have another effect in the real world, which must be parameterized in FLOR: their transient vertical shears enhance vertical mixing near the equator, which may offset much of their rectified warming effect from meridional stirring (Lien et al. 2008; Moum et al. 2009; Holmes and Thomas 2015). These competing effects were evident in Figs. 2b and 2d (blue and green curves) of Part I of this study, which showed enhanced vertical diffusive cooling in FLOR during the period of strongest advective warming, just prior to the arrival of a TIW warm trough.

b. Vertical mixing in the equatorial cold tongue

Figure 10 shows the vertical structure of the time-mean $\overline{T}$, $\partial_z \overline{T}$, $\overline{u}$, $\partial_z \overline{u}$, $\overline{\kappa_z}$, and vertical diffusive heat flux, on the

equator at 125°W. Compared to SODA, FLOR produces very realistic profiles of $\overline{T}$ and $\partial_z \overline{T}$, although FLOR's thermocline (peak $\partial_z \overline{T}$) is about 30 m too shallow, and FLOR's EUC is only slightly weaker and deeper than SODA's. FLOR shows strong $\overline{\kappa_z}$ near the surface and weak $\overline{\kappa_z}$ at 110 m near the core of the EUC.

FLOR's time-mean downward vertical diffusive heat flux (i.e., the time mean of the hourly κ_z from the ocean model; solid red line in Fig. 10f), converges strongly between 30- and 80-m depth. The vertical diffusive heat transport near the surface is greatly suppressed by the submonthly anticorrelation between κ_z and $\partial_z T$: Fig. 10f shows that omitting this submonthly covariation, by using only monthly-mean κ_z and $\partial_z T$ to compute the heat flux (dashed red line), would severely overestimate the actual time-mean downward heat flux and its convergence within the top 40 m. This is because as the surface-intensified submonthly stirring generates transient κ_z and $\partial_z T$, regions with strong stratification tend to suppress local vertical mixing, while regions with strong vertical mixing tend to erode local stratification.

Compared to FLOR, FLOR-FA's deeper thermocline results in a prominent warm bias below 30 m, with FLOR-FA's $\partial_z \overline{T}$ being too weak above 100 m and too strong below 100 m. FLOR-FA's stronger $\overline{\kappa_z}$ relative to FLOR above 90 m is attributable to FLOR-FA's weaker stratification. FLOR-FA's deeper EUC core also produces a deeper minimum in $\overline{\kappa_z}$, which allows FLOR-FA to maintain stronger $\partial_z \overline{u}$ and $\overline{\kappa_z}$ between 90 and 120 m, despite stronger $\partial_z \overline{T}$ in that depth range.

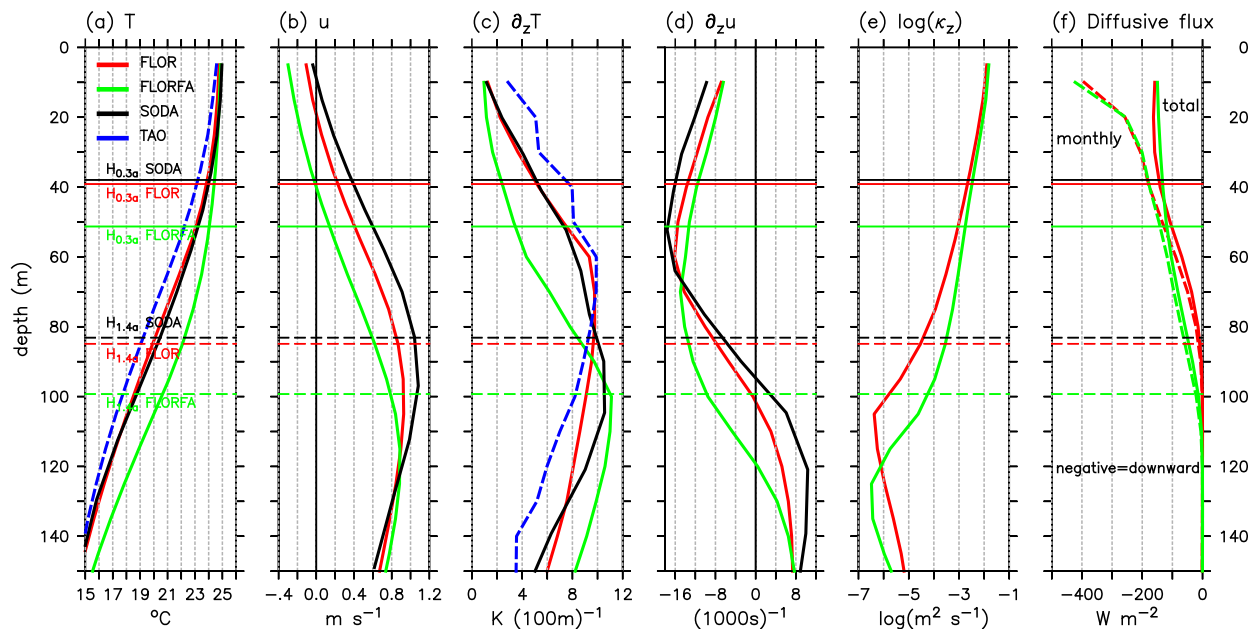## Vertical profiles on the equator at 125°W

FIG. 10. Climatological annual-mean profiles on the equator at 125°W of (a) temperature T (°C), (b) zonal current u (m s^{-1}), (c) vertical temperature gradient $\partial_z T$ [K (100 m)$^{-1}$], (d) zonal current vertical shear $\partial_z u$ [(1000 s)$^{-1}$], (e) log of the vertical thermal diffusivity κ_z (m^2 s^{-1}), and (f) local diffusive heat flux (W m^{-2}; negative downward) due to vertical mixing. Results are shown for TAO (1980–2010; blue), SODA 2.2.4 (1980–2010; black), FLOR (30 yr; red), and FLOR-FA (30 yr; green). Horizontal lines indicate the SML depth $H_{0.3a}$ (solid) and AL depth (dashed) $H_{1.4a}$ on the equator at 125°W for SODA, FLOR, and FLOR-FA. In (f) the solid curves indicate the time mean of the hourly diffusive heating actually diagnosed by the FLOR ocean model, while dashed curves indicate the "monthly vertical diffusive flux," namely the time mean of the product of monthly-mean κ_z and monthly-mean $\partial_z T$; T, u, and κ_z are diagnosed at the vertical center of each model grid cell, while $\partial_z T$, $\partial_z u$, and the vertical diffusive heat flux are diagnosed at the bottom of each cell.

Interestingly, above 50 m the FA has little effect on the monthly and submonthly components of FLOR's vertical diffusive heat flux. However, the FA allows the diffusive heat fluxes to penetrate deeper, leading to a deeper zone of flux convergence and diffusive heating, which then must be balanced by the deeper monthly advective cooling associated with FLOR-FA's deeper thermocline.

8. Discussion

We have examined a coupled GCM, GFDL-FLOR, that captures the intensity and structure of the ECT SST better than most other coupled GCMs, nearly eliminating the equatorial cold bias that plagues most other models. Our examination of the ECT temperature budget reveals that FLOR's realistic ECT structure results partly from cancelling errors. Compared to the SODA reanalysis, FLOR appears to show an excessive stratifying effect from deep equatorial monthly-scale vertical advective cooling, which is induced by overly cyclonic off-equatorial wind stress curl. This effect is then compensated by weakened stratifying effects from

submonthly processes (including TIWs) and/or a strengthened destratifying effect of vertical mixing in the upper ocean.

These results highlight the need to look beyond simple emergent characteristics (such as the climatological SST and thermocline depth fields) when evaluating a climate model; it is critical to also examine the underlying ocean dynamics and processes. A model with cancelling errors can look excellent in some respects, but can harbor hidden weaknesses that might then alter ENSO feedbacks or the climate response to external radiative forcings. As an example, FLOR's excessive dependence on deep vertical advective cooling and weak TIWs to maintain its realistic mean thermal stratification at the equator could make FLOR's SST too sensitive to thermocline depth *fluctuations*—especially during La Niña when the thermocline shoals—contributing to FLOR's intense La Niña events and insufficient positive skewness of ECT SSTs (Wittenberg et al. 2018).

Compensating errors can also create a tortuous path toward better models, since ameliorating one dynamical bias may actually *degrade* overall model performance, until the formerly compensating bias(es) can be addressed

as well. Work is underway to evaluate the broader tropical Pacific climate of our flux-adjusted simulation (FLOR-FA). FLOR-FA suggests that to improve FLOR, it is not enough to simply correct the model's climatological surface heat fluxes and wind stresses, since this leaves unchecked the excessive submonthly destratification, which then overdeepens the equatorial thermocline. We therefore advocate a coordinated approach to simultaneously improve the off-equatorial wind stress curl, intraseasonal variability (including TIWs and wind-driven equatorial Kelvin waves), and vertical mixing parameterizations in tandem, using the ocean heat budget as a guide.

To enable evaluations of GCM heat budgets, improved constraints are needed from both in situ observations and ocean reanalyses, especially for the submonthly and diurnal components of the ocean temperature budget. Our analysis of FLOR indicates that the monthly vertical advection, diffusive vertical mixing, and TIW activity are all particularly strong during La Niña years and boreal summer/autumn, and the downward diffusive heat transport is also particularly strong at night. The TPOS2020 project (Cravatte et al. 2016) has proposed several enhancements of the tropical Pacific observing system that could help constrain those regimes and phenomena, including denser in situ sampling of ocean temperatures, salinity, currents, and surface heat fluxes especially near the equator. Our study suggests that submonthly sampling (at least every 5 days), with sufficient vertical refinement to resolve the TIW-induced variations in vertical shear within the oceanic mixed layer, will be needed to constrain important TIW effects on upwelling, mixing, and stirring as a function of the seasonal cycle and ENSO. Better constraints are also needed for the diurnal cycle of upper-ocean temperatures and mixing, via focused field studies and perhaps sustained monitoring.

In addition to enhanced measurements, it would be very helpful for future ocean reanalyses to provide their simulated upwelling velocities, vertical diffusive heat fluxes, parameterized diffusivities, and the full time-mean temperature budget for the upper ocean—evaluated using high-frequency (hourly or daily) temperatures and currents—as these are very difficult to obtain directly from in situ measurements. It is also important for ocean reanalyses to provide the thermal sources and sinks induced by their temperature corrections toward observations to ensure that the heat budget closes diagnostically.

The monthly/submonthly (30 day) split that we have used here is not ideal when it comes to TIWs, which typically exhibit periods of 20–30 days (McPhaden et al. 1998). For future work, we would therefore recommend a seasonal/subseasonal (90 day) split, so that TIW activity is more fully contained within the high-frequency band. To

better isolate the TIW component, it may even be helpful to use a two-dimensional bandpass filter in both longitude and time to more cleanly extract westward-propagating TIW signals (e.g., Wittenberg et al. 2018). One could even apply several such filters to isolate other physical phenomena, such as intraseasonal equatorial Kelvin waves driven by intraseasonal westerly wind burst activity in the western and central Pacific. Such studies would be very helpful for model developers, as they would help isolate particular physical processes (e.g., subsurface mixing processes, representation of TIW fronts, surface wind stress variability in the atmosphere, etc.) that are controlled by particular subgrid-scale parameterizations.

Additional analysis of TIW-resolving, high-resolution ocean models, such as CM2.6, could clarify the extent to which TIWs act to stratify (via submonthly meridional stirring) or destratify (via submonthly shear-driven vertical mixing) the ECT. This would help to constrain the impacts of TIWs on the ECT temperature budget and ocean heat uptake, and foster the development of improved TIW parameterizations for use in the lower-resolution coupled climate models used for seasonal-to-decadal forecasts and future projections. Additional constraints on the destratifying effects of submonthly vertical mixing (including that induced by TIWs) and shortwave penetration, both on- and off-equator, would also be very helpful to improve the equatorial thermal structure in climate models.

Although the present study has focused on the Pacific ECT region, our temperature budget framework can and should be adapted to study other regions, such as the west Pacific warm pool, the east Pacific upwelling zone near South America, and the tropical Indian and Atlantic basins. It would also be interesting to examine the temporal evolution of temperature budget biases in seasonal forecast runs, to further isolate the time scales and processes contributing to coupled model errors.

9. Summary

The heat budget of the Pacific equatorial cold tongue (ECT) was explored using the GFDL-FLOR coupled GCM and ocean reanalyses, leveraging the two-layer framework developed in Part I of this study.

Despite FLOR's relatively weak meridional stirring by tropical instability waves (TIWs), the model maintains a reasonable SST and thermocline depth in the ECT via two compensating biases: 1) enhanced monthly-scale vertical advective cooling below the surface mixed layer (SML), due to overly cyclonic off-equatorial wind stress that acts to cool the equatorial source waters, and 2) an excessive SST contrast between the ECT and off-equator areas, which boosts the equatorward heat transport by TIWs. FLOR's strong advective cooling at the
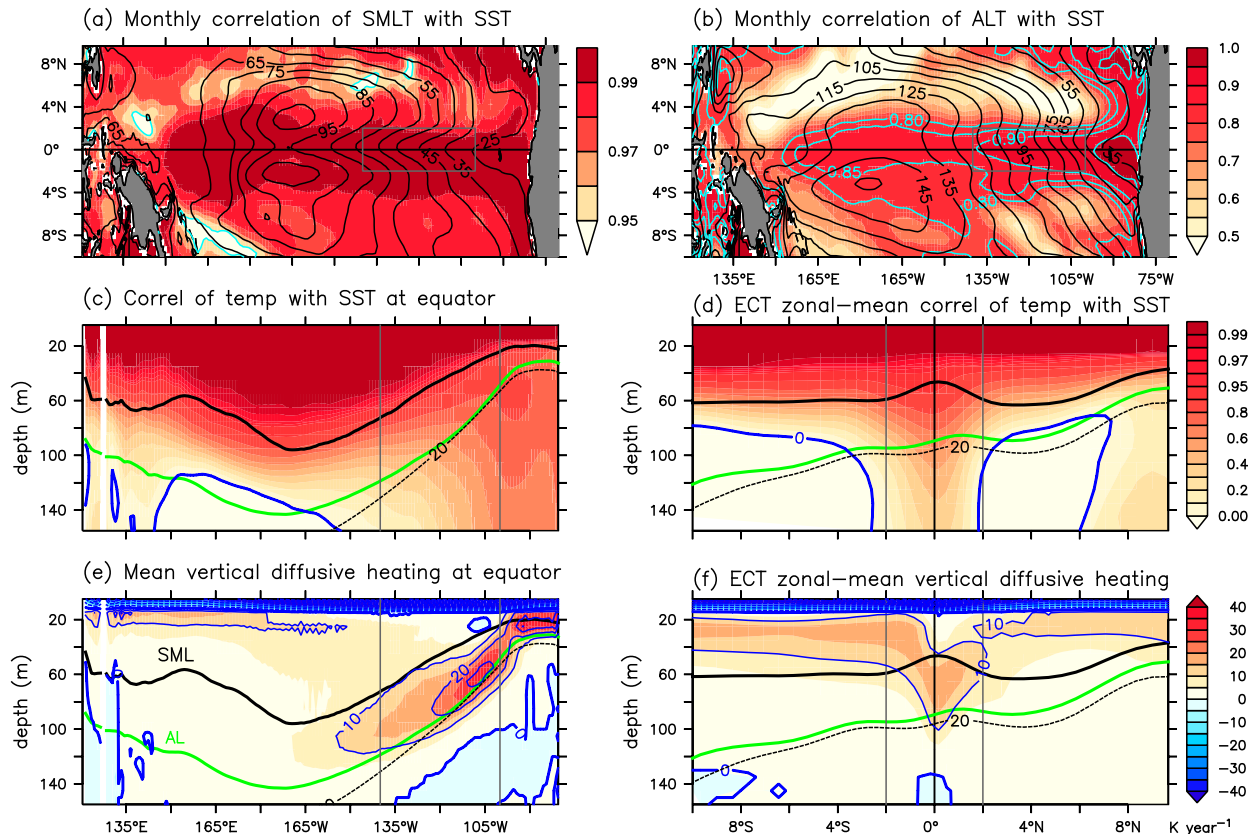
FIG. A1. Layer structures in the 30-yr FLOR-FA control simulation, for comparison with FLOR in Fig. 5 of Part I of this paper. (a) Local correlation (shaded) between the monthly-mean SST and the monthly-mean temperature ($T_{0.3a}$) of a stationary surface mixed layer (SML) whose thickness ($H_{0.3a}$) is indicated by the black contours. (b) As in (a), but for the monthly-mean temperature ($T_{1.4a}$) of an advective layer (AL) with thickness $H_{1.4a}$. Light blue contours indicate correlations of 0.8, 0.85, 0.9, and 0.95. (c) Equatorial correlation between monthly-mean temperature and monthly-mean SST, SML depth (thick black curve), AL depth (solid green curve), and 20°C isotherm depth (thin dashed black curve). (d) As in (c), but correlations are now zonally averaged between 140° and 100°W. (e) As in (c), but shading is now the equatorial time-mean vertical diffusive heating (blue contours, with shading incremented every half-contour). (f) As in (e), but diffusive heating is now zonally averaged between 140° and 100°W. The ECT region is indicated by a gray box in (a),(b), and gray vertical lines in (c)–(f).

SML base is compensated by strong downward diffusion of heat out of the SML, which then allows FLOR's ECT to take up a realistic heat flux from the atmosphere.

Correcting FLOR's climatological SST and wind stress biases via flux adjustment (FA) leads to weaker deep advective cooling of the ECT, which then erodes the upper-ocean thermal stratification, enhances vertical mixing, and excessively deepens FLOR's thermocline. The temperature budget suggests that FLOR-FA's deep thermocline is linked to excessive downward diffusive transport of heat at the equator, due to an inherent bias in the vertical mixing formulation and/or weak TIWs at this ocean resolution, which may lead to insufficient restratification from subseasonal lateral stirring (a warming effect near the surface at the equator) and transient vertical mixing (a cooling effect at the base of the SML).

FA does strengthen FLOR's meridional shear of the zonal currents in the east Pacific, but this does not amplify the simulated TIWs nor their equatorward heat transport. An experiment (CM2.6) with refined ocean resolution exhibits much stronger TIW heat transport, suggesting that FLOR's coarse ocean resolution may be limiting its simulated TIW activity.

These results suggest that to advance coupled simulations of the ECT, improved simulations of the tropical Pacific surface winds and surface heat fluxes will need to go hand in hand with better representations of submonthly and parameterized ocean processes. Improved observations (e.g., the Tropical Pacific Observing System), ocean reanalyses, and higher-resolution simulations will be essential to support future progress toward simulating and predicting the climate and variability of the tropical Pacific, and their impacts on the global climate system.
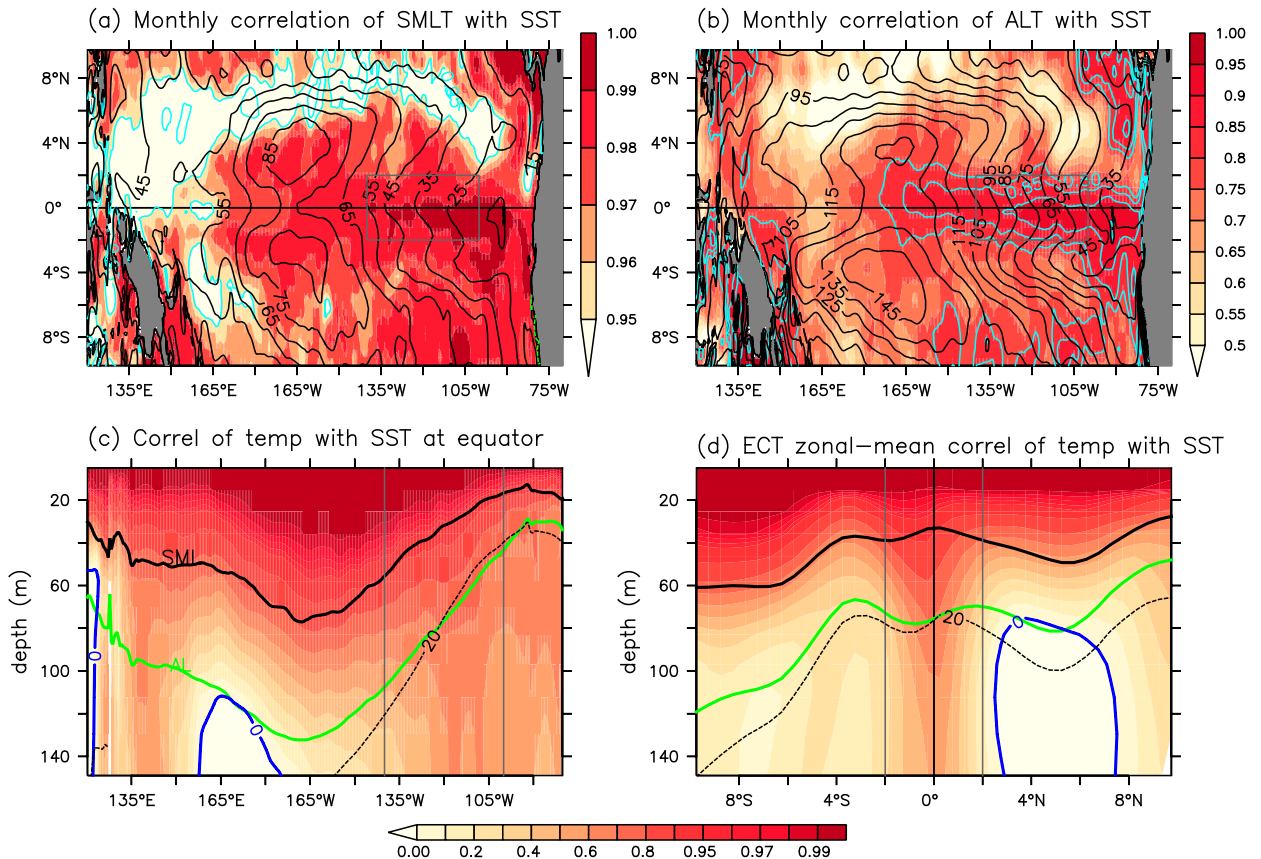
FIG. A2. As in Figs. A1a–d, but for SODA.

APPENDIX A

Two-Layer Decomposition for FLOR-FA and SODA

As discussed in section 4 of Part I, it is desirable for the SML to be shallow enough that its temperature is highly correlated with SST. Figure A1a shows that for FLOR-FA, the correlation between monthly-mean SST and $T_{0.3a}$ exceeds 95% over most of the basin, and 98% within the ECT. Figure A2a for SODA shows somewhat lower correlations, especially under the zones of atmospheric deep convection (west Pacific, ITCZ, and SPCZ), possibly due to observational SST corrections in the SODA

reanalysis that are disconnected with the subsurface temperatures. However, within the ECT the correlations are quite high even for SODA, exceeding 98%.

Comparing Figs. A1 and A2 to the analogous figure for FLOR (Fig. 5 in Part I) confirms that the SML, AL, and ADL layers defined using $H_{0.3a}$ and $H_{1.4a}$ track similar regimes in FLOR-FA and SODA as in FLOR, especially in the ECT. Namely, $T_{0.3a}$ is highly correlated with SST, the AL base tracks the thermocline within the ECT, and the ADL brackets the zone of maximum vertical diffusive heating. Note that SODA does not provide a diffusive heating diagnostic, so we cannot fully assess the ADL budget as we do for the FLOR and FLOR-FA simulations.

As discussed in section 6, the SML and AL have different thicknesses in SODA, FLOR, and FLOR-FA. An advantage of our density-based (rather than depth-based) layer framework is that it accounts for the impact of these depth changes on the layer budgets—in particular the role of the surface heat fluxes relative to the subsurface terms. Section 6 and Fig. 7 examine the impact of the layer changes on the heat budgets of FLOR and FLOR-FA, relative to SODA.

Equatorial zonal current (cm s⁻¹)
annual mean
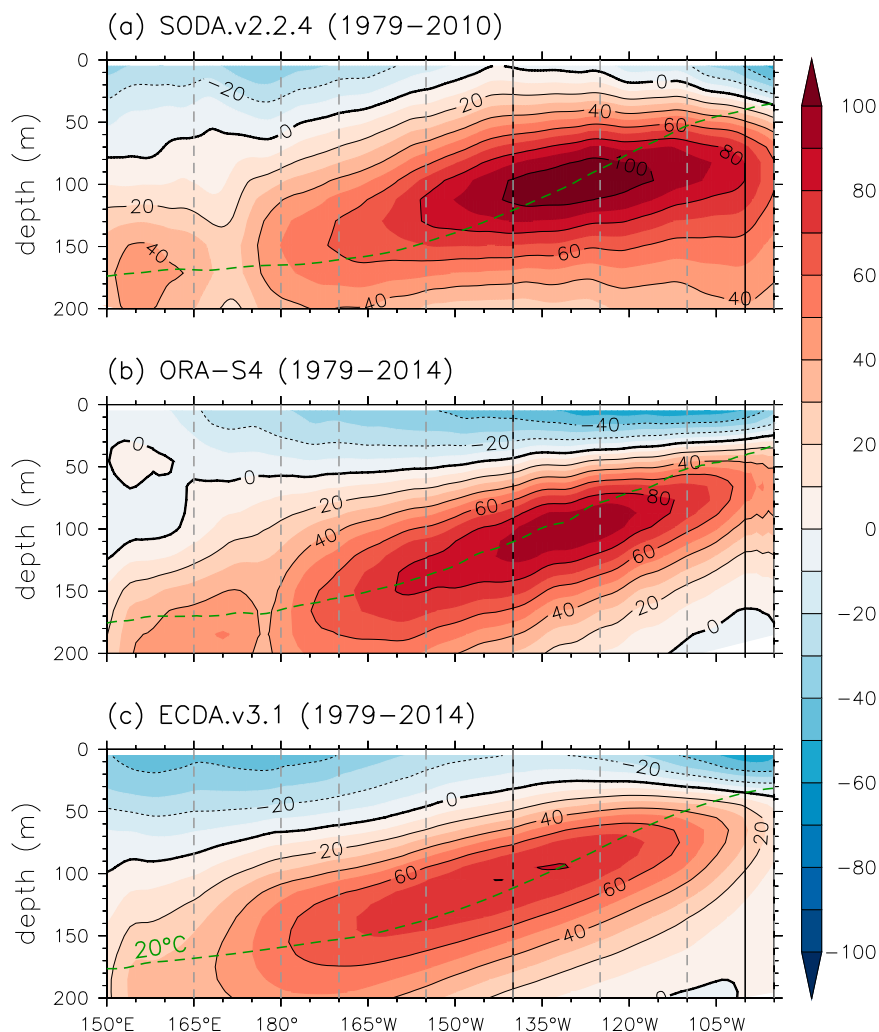

FIG. B1. Climatological annual-mean zonal current velocity (cm s⁻¹), interpolated to the equator within the Pacific upper ocean, from three model-based reanalyses of observations: (a) SODA.v2.2.4 (averaged 1979–2010), (b) ORA-S4 (averaged 1979–2014; Balmaseda et al. 2013), and (c) ECDA.v3.1 (averaged 1979–2014; Chang et al. 2013). Shading is incremented every half-contour. Dashed green curve indicates the depth of the 20°C isotherm, diagnosed from the time-mean climatological temperature field for each reanalysis. Vertical gray dashed lines indicate the longitudes of the equatorial TAO moorings. Vertical black lines indicate the boundaries of the ECT region analyzed in this study.

APPENDIX B

Time-Mean Equatorial Currents in Ocean Reanalyses

Figure B1 shows the equatorial Pacific climatological annual-mean zonal current velocity estimates from the SODA.v2.2.4, ORA-S4, and ECDA.v3.1 ocean re-analyses. All three products exhibit a westward SEC at the surface, and an eastward EUC that slopes upward from west to east (somewhat less steeply than the 20°C isotherm), peaking near 130°W at about 100-m depth. Yet there are also large differences among the rean-alyses. SODA produces the weakest SEC at the sur-face, and the strongest subsurface EUC with a peak of just over 100 cm s⁻¹. East of 125°W the EUC is vertically broader in SODA than the other reanalyses, and the EUC core lies well below the 20°C isotherm at 100°E

Equatorial upwelling (m day^{-1})
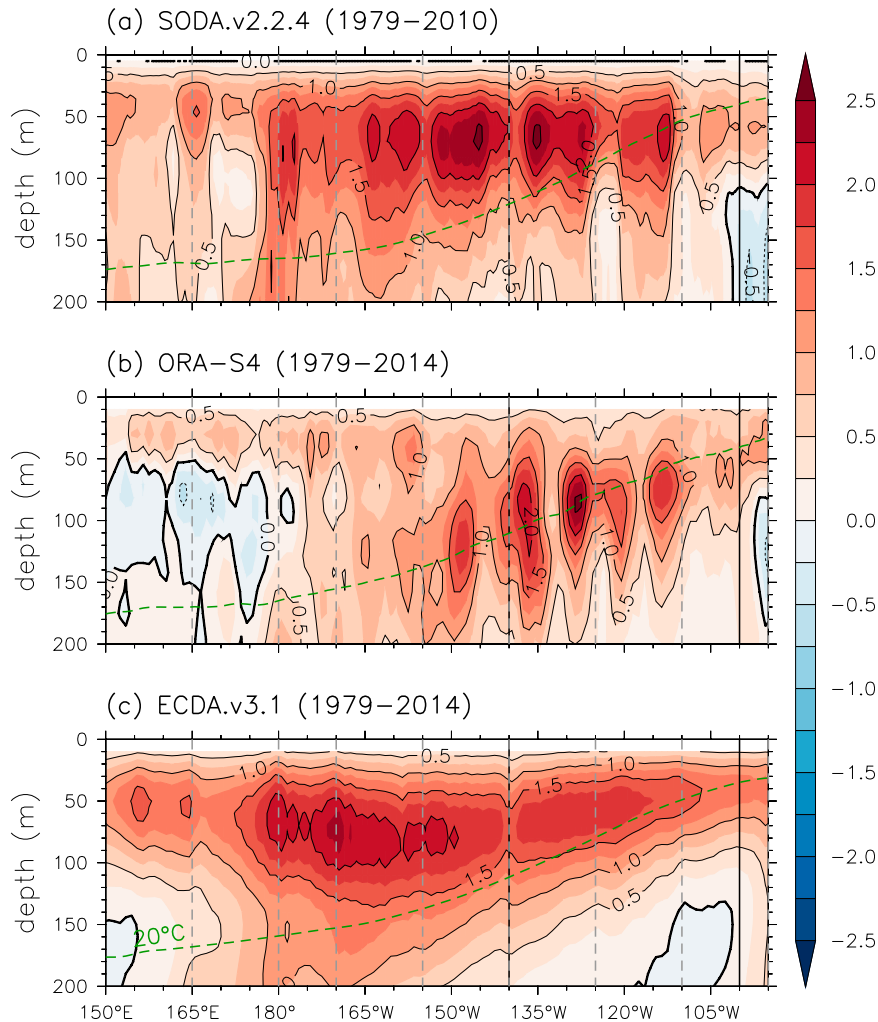### annual mean

FIG. B2. As in Fig. B1, but for the vertical velocity (m day^{-1}).

(the eastern edge of the ECT region). In contrast, ORA-S4 has a stronger westward SEC than SODA, and a slightly weaker EUC that is more narrowly confined in the vertical and slopes more steeply up from west to east, with the EUC core closer to the 20° isotherm. ECDA. v3.1 has the weakest EUC, with a peak farther west than SODA or ORA-S4.

Figure B2 shows the equatorial Pacific climatological annual-mean vertical velocity estimates from the three reanalyses. The upwelling differences among the reanalyses are far larger than the zonal current differences shown in Fig. B1. All three reanalyses (especially SODA and ORA-S4) exhibit localized persistent spikes in the upwelling along the equator, likely associated

with imperfect assimilation of sparse TAO mooring data into models with equatorial biases; these biases stem from ocean model physics errors and/or errors in the surface flux forcings (wind stress, heat, and freshwater) used to drive the model. SODA's upwelling, which is strongest at 70-m depth, spans a broad swath of the basin between 180° and 110°W and is not much shallower in the ECT than farther west. In contrast, ORA-S4's upwelling is much deeper, concentrated near the 20°C isotherm and between 155° and 110°W. ECDA.v3.1 differs as well, with a zonally smoother upwelling field that spans a broad swath between 175°E and 110°W, sloping downward to the west approaching its peak near 170°W.
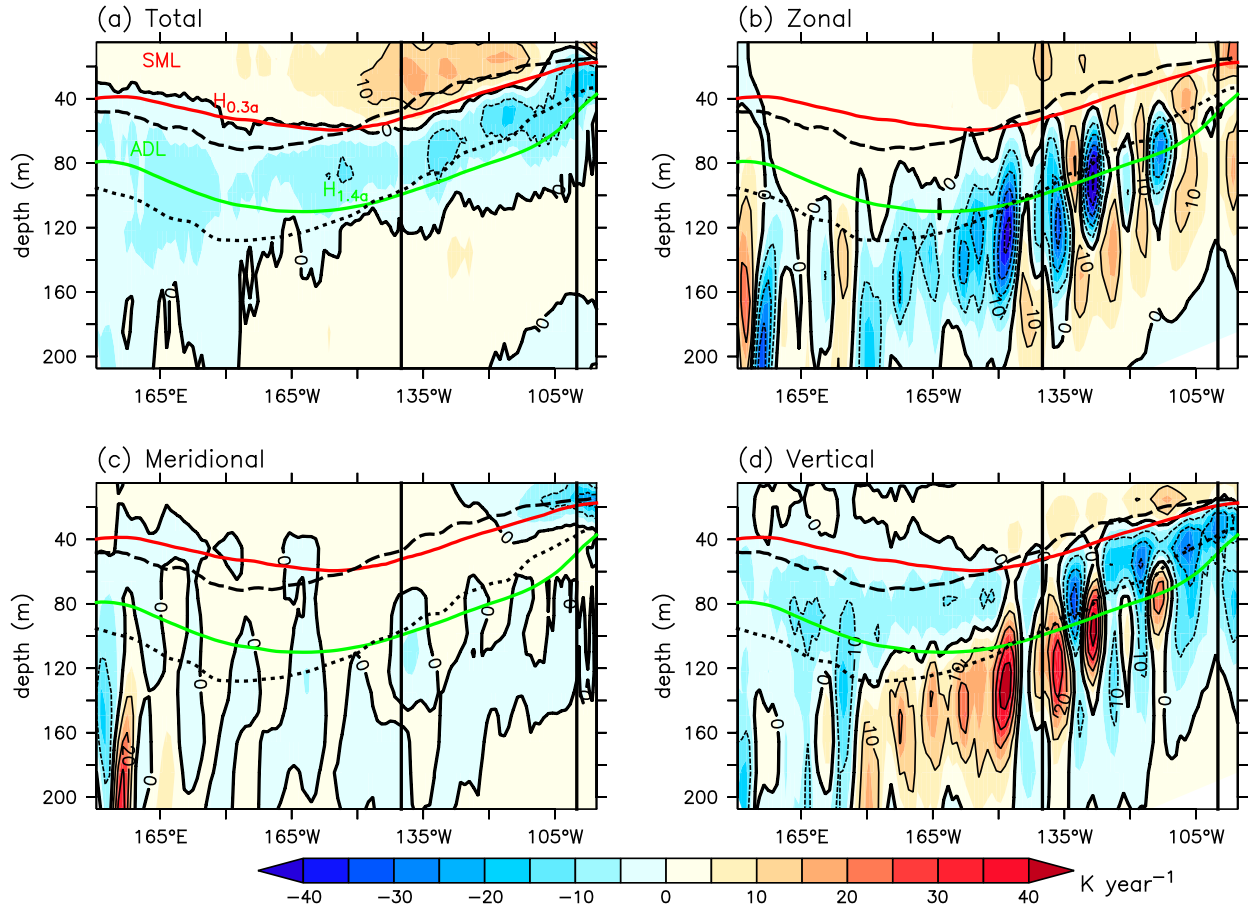
FIG. C1. As in Fig. 2, but for FLOR's difference from the ORA-S4 reanalysis (1980–2010; Balmaseda et al. 2013).

The large differences in equatorial currents and up-welling among these ocean assimilation products high-lights a continuing need for improved observations and reanalyses to better constrain simulations of the equatorial Pacific currents. This is one of the thrusts of the TPOS2020 project (Cravatte et al. 2016), which has proposed denser sampling of the near-equatorial currents in the equatorial cold tongue region. Intercomparisons of the reanalysis models, parameterizations, forcings, and assimilation methods could also help to resolve these large disparities in the structure and variability of the equatorial currents, and improve understanding of the roles of the currents in the heat budget of the equatorial Pacific.

APPENDIX C

Monthly-Scale Advection in FLOR Relative to Ocean Reanalyses

Figure C1 shows the equatorial Pacific climatological annual-mean monthly-scale advective components, for the FLOR simulation minus the ORA-S4 reanalysis. As in the comparison with SODA (Fig. 2), FLOR's ECT AL shows a stronger stratifying influence of monthly zonal advective heating and vertical advective cooling. In Fig. C1 this is due to FLOR having both less SML cooling and more ADL cooling than ORA-S4; but in Fig. 2 it was mainly due to FLOR having more ADL cooling than SODA. Like SODA, ORA-S4 also exhibits localized spikes of vertical advection along the equator (Fig. C1d) due to spiky upwelling features near the moorings (Fig. B2b), which likely arise from imperfect assimilation of zonally sparse TAO mooring data. However, in ORA-S4 these vertical advective spikes are largely countered by opposing spikes in zonal advection (Fig. C1b), leading to a relatively smooth total monthly advection field (Fig. C1a).

As in Figs. 2 and C1, Fig. C2 also shows a stronger ECT-stratifying influence of monthly zonal advective warming and vertical advective cooling, in FLOR relative to ECDA.v3.1. Fig. C2d indicates that west of the ECT, FLOR has much weaker vertical advective cooling
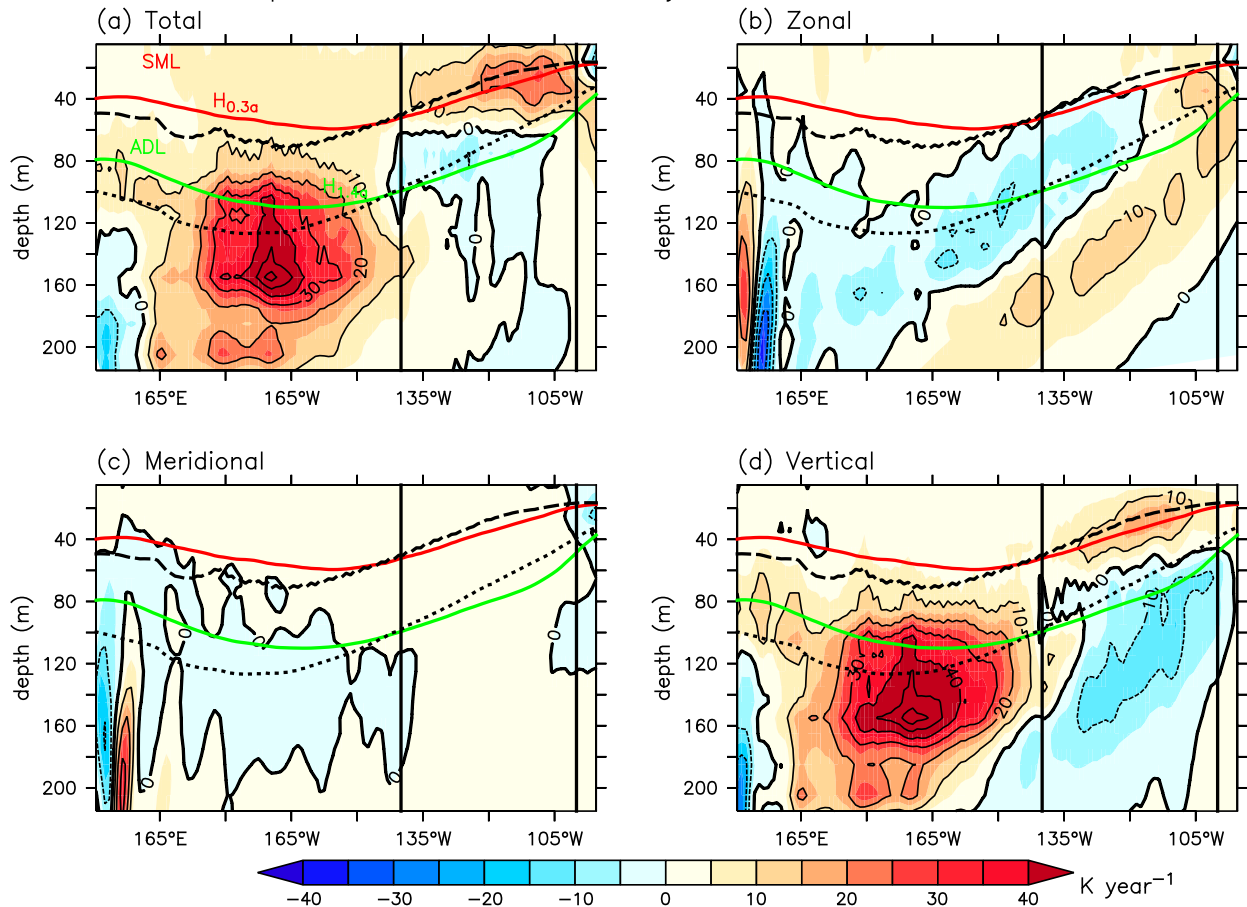
FIG. C2. As in Fig. 2, but for FLOR's difference from the GFDL-ECDA.v3.1 reanalysis (1980–2010; Chang et al. 2013).

below the AL; this is also seen in Fig. 2d and to a lesser extent in Fig. C1d. In ECDA the time-mean vertical advection is much smoother than in SODA and ORA-S4, without the spiky features seen in those reanalyses.

Figures 2, C1, and C2 exemplify the large differences in ocean reanalysis heat budgets, which can complicate the diagnosis of model biases. Improved heat budget constraints are clearly needed, and it is hoped that the TPOS2020 effort (Cravatte et al. 2016) will provide these in the future. However, all three figures do suggest that FLOR's monthly-scale vertical and zonal advective terms are working too hard to stratify the ECT active layer, possibly to compensate for a lack of sufficient restratification by TIWs and/or excessive destratification by parameterized vertical mixing.

REFERENCES

Anderson, W., A. Gnanadesikan, R. Hallberg, J. Dunne, and B. Samuels, 2007: Impact of ocean color on the maintenance of the Pacific cold tongue. *Geophys. Res. Lett.*, **34**, L11609, https://doi.org/10.1029/2007GL030100.

Balmaseda, M. A., K. Mogensen, and A. T. Weaver, 2013: Evaluation of the ECMWF ocean reanalysis system ORAS4. *Quart. J. Roy. Meteor. Soc.*, **139**, 1132–1161, https://doi.org/10.1002/qj.2063.

Banzon, V., T. M. Smith, T. M. Chin, C. Liu, and W. Hankins, 2016: A long-term record of blended satellite and in situ sea-surface temperature for climate monitoring, modeling and environmental studies. *Earth Syst. Sci. Data*, **8**, 165–176, https://doi.org/10.5194/essd-8-165-2016.

Burls, N., and A. Fedorov, 2014: What controls the mean east–west sea surface temperature gradient in the equatorial Pacific: The role of cloud albedo. *J. Climate*, **27**, 2757–2778, https://doi.org/10.1175/JCLI-D-13-00255.1.

Cai, W., and Coauthors, 2014: Increasing frequency of extreme El Niño events due to greenhouse warming. *Nat. Climate Change*, **4**, 111–116, https://doi.org/10.1038/nclimate2100.

Capotondi, A., Y.-G. Ham, A. T. Wittenberg, and J.-S. Kug, 2015: Climate model biases and El Niño Southern Oscillation (ENSO) simulation. U.S. CLIVAR Variations, Vol. 13, U.S. CLIVAR Program Office, Washington, D.C., 21–25, https://extranet.gfdl.noaa.gov/~atw/yr/2015/capotondi_etal_variations2015.pdf.

Chang, P., 1996: The role of the dynamic ocean–atmosphere interactions in tropical seasonal cycle. *J. Climate*, **9**, 2973–2985, https://doi.org/10.1175/1520-0442(1996)009<2973:TROTDO>2.0.CO;2.

Chang, Y.-S., S. Zhang, A. Rosati, T. L. Delworth, and W. F. Stern, 2013: An assessment of oceanic variability for 1960–2010 from

the GFDL Ensemble Coupled Data Assimilation. *Climate Dyn.*, **40**, 775–803, https://doi.org/10.1007/s00382-012-1412-2.

Cravatte, S., and Coauthors, 2016: First Report of TPOS 2010. Tech. Rep. GOOS-215, 200 pp., http://tpos2020.org/first-report/.

Dai, A., 2006: Precipitation characteristics in eighteen coupled climate models. *J. Climate*, **19**, 4605–4630, https://doi.org/10.1175/JCLI3884.1.

Dee, D. P., and Coauthors, 2011: The ERA-Interim reanalysis: Configuration and performance of the data assimilation system. *Quart. J. Roy. Meteor. Soc.*, **137**, 553–597, https://doi.org/10.1002/qj.828.

Delworth, T. L., and Coauthors, 2012: Simulated climate and climate change in the GFDL CM2.5 high-resolution coupled climate model. *J. Climate*, **25**, 2755–2781, https://doi.org/10.1175/JCLI-D-11-00316.1.

de Szoeke, S. P., and S.-P. Xie, 2008: The tropical eastern Pacific seasonal cycle: Assessment of errors and mechanisms in IPCC AR4 coupled ocean–atmosphere general circulation models. *J. Climate*, **21**, 2573–2590, https://doi.org/10.1175/2007JCLI1975.1.

Eyring, V., S. Bony, G. A. Meehl, C. A. Senior, B. Stevens, R. J. Stouffer, and K. E. Taylor, 2016: Overview of the Coupled Model Intercomparison Project Phase 6 (CMIP6) experimental design and organization. *Geosci. Model Dev.*, **9**, 1937–1958, https://doi.org/10.5194/gmd-9-1937-2016.

Giese, B. S., and S. Ray, 2011: El Niño variability in Simple Ocean Data Assimilation (SODA), 1871–2008. *J. Geophys. Res.*, **116**, C02024, https://doi.org/10.1029/2010JC006695.

Graham, F., A. T. Wittenberg, J. N. Brown, S. J. Marsland, and N. J. Holbrook, 2017: Understanding the double peaked El Niño in coupled GCMs. *Climate Dyn.*, **48**, 2045–2063, https://doi.org/10.1007/s00382-016-3189-1.

Griffies, S. M., and Coauthors, 2015: Impacts on ocean heat from transient mesoscale eddies in a hierarchy of climate models. *J. Climate*, **28**, 952–977, https://doi.org/10.1175/JCLI-D-14-00353.1.

Guilyardi, E., A. Wittenberg, M. Balmaseda, W. Cai, M. Collins, M. J. McPhaden, M. Watanabe, and S.-W. Yeh, 2016: Fourth CLIVAR workshop on the evaluation of ENSO processes in climate models: ENSO in a changing climate. *Bull. Amer. Meteor. Soc.*, **97**, 817–820, https://doi.org/10.1175/BAMS-D-15-00287.1.

Ham, Y.-G., and J.-S. Kug, 2012: How well do current climate models simulate two types of El Niño? *Climate Dyn.*, **39**, 383–398, https://doi.org/10.1007/s00382-011-1157-3.

Holmes, R. M., and L. N. Thomas, 2015: The modulation of equatorial turbulence by tropical instability waves in a regional ocean model. *J. Phys. Oceanogr.*, **45**, 1155–1173, https://doi.org/10.1175/JPO-D-14-0209.1.

Inoue, R., R.-C. Lien, and J. Moum, 2012: Modulation of equatorial turbulence by a tropical instability wave. *J. Geophys. Res.*, **117**, C10009, https://doi.org/10.1029/2011JC007767.

Jia, Y., R. Furue, and J. P. McCreary, 2015: Impacts of regional mixing on the temperature structure of the equatorial Pacific Ocean. Part 2: Depth-dependent vertical diffusion. *Ocean Modell.*, **91**, 112–127, https://doi.org/10.1016/j.ocemod.2015.02.007.

Jochum, M., R. Murtugudde, R. Ferrari, and P. Malanotte-Rizzoli, 2005: The impact of horizontal resolution on the tropical heat budget in an Atlantic Ocean model. *J. Climate*, **18**, 841–851, https://doi.org/10.1175/JCLI-3288.1.

——, M. F. Cronin, W. S. Kessler, and D. Shea, 2007: Observed horizontal temperature advection by tropical instability waves. *Geophys. Res. Lett.*, **34**, L09604, https://doi.org/10.1029/2007GL029416.

Kug, J.-S., Y.-G. Ham, J.-Y. Lee, and F.-F. Jin, 2012: Improved simulation of two types of El Niño in CMIP5 models. *Environ. Res. Lett.*, **7**, 034002, https://doi.org/10.1088/1748-9326/7/3/034002.

Li, G., and S.-P. Xie, 2012: Origins of tropical-wide SST biases in CMIP multi-model ensembles. *Geophys. Res. Lett.*, **39**, L22703, https://doi.org/10.1029/2012GL053777.

——, and ——, 2014: Tropical biases in CMIP5 multimodel ensemble: The excessive equatorial Pacific cold tongue and double ITCZ problems. *J. Climate*, **27**, 1765–1780, https://doi.org/10.1175/JCLI-D-13-00337.1.

Lien, R.-C., E. A. D'Asaro, and C. E. Menkes, 2008: Modulation of equatorial turbulence by tropical instability waves. *Geophys. Res. Lett.*, **35**, L24607, https://doi.org/10.1029/2008GL035860.

Liu, C., A. Köhl, Z. Liu, F. Wang, and D. Stammer, 2016: Deep-reaching thermocline mixing in the equatorial Pacific cold tongue. *Nat. Commun.*, **7**, 11576, https://doi.org/10.1038/ncomms11576.

McPhaden, M. J., and Coauthors, 1998: The Tropical Ocean–Global Atmosphere observing system: A decade of progress. *J. Geophys. Res.*, **103**, 14 169–14 240, https://doi.org/10.1029/97JC02906.

Mechoso, C. R., and Coauthors, 1995: The seasonal cycle over the tropical Pacific in coupled ocean–atmosphere general circulation models. *Mon. Wea. Rev.*, **123**, 2825–2838, https://doi.org/10.1175/1520-0493(1995)123<2825:TSCOTT>2.0.CO;2.

Menkes, C. E., J. G. Vialard, S. C. Kennan, J.-P. Boulanger, and G. V. Madec, 2006: A modeling study of the impact of tropical instability waves on the heat budget of the eastern equatorial Pacific. *J. Phys. Oceanogr.*, **36**, 847–865, https://doi.org/10.1175/JPO2904.1.

Moum, J. N., R.-C. Lien, A. Perlin, J. Nash, M. Gregg, and P. Wiles, 2009: Sea surface cooling at the equator by subsurface mixing in tropical instability waves. *Nat. Geosci.*, **2**, 761–765, https://doi.org/10.1038/ngeo657.

——, A. Perlin, J. D. Nash, and M. J. McPhaden, 2013: Seasonal sea surface cooling in the equatorial Pacific cold tongue controlled by ocean mixing. *Nature*, **500**, 64–67, https://doi.org/10.1038/nature12363.

Power, S., F. Delage, C. Chung, G. Kociuba, and K. Keay, 2013: Robust twenty-first-century projections of El Niño and related precipitation variability. *Nature*, **502**, 541–545, https://doi.org/10.1038/nature12580.

Praveen Kumar, B., J. Vialard, M. Lengaigne, V. Murty, and M. McPhaden, 2012: TropFlux: Air–sea fluxes for the global tropical oceans—Description and evaluation. *Climate Dyn.*, **38**, 1521–1543, https://doi.org/10.1007/s00382-011-1115-0.

Qiao, L., and R. H. Weisberg, 1995: Tropical instability wave kinematics: Observations from the tropical instability wave experiment. *J. Geophys. Res.*, **100**, 8677–8693, https://doi.org/10.1029/95JC00305.

Ray, S., A. T. Wittenberg, S. M. Griffies, and F. Zeng, 2018: Understanding the equatorial Pacific cold tongue time-mean heat budget. Part I: Diagnostic framework. *J. Climate*, **31**, 9965–9985, https://doi.org/10.1175/JCLI-D-18-0152.1.

Rayner, N., D. E. Parker, E. Horton, C. Folland, L. Alexander, D. Rowell, E. Kent, and A. Kaplan, 2003: Global analyses of sea surface temperature, sea ice, and night marine air temperature since the late nineteenth century. *J. Geophys. Res.*, **108**, 4407, https://doi.org/10.1029/2002JD002670.

Swenson, M. S., and D. V. Hansen, 1999: Tropical Pacific Ocean mixed layer heat budget: The Pacific cold tongue. *J. Phys. Oceanogr.*, **29**, 69–81, https://doi.org/10.1175/1520-0485(1999)029<0069:TPOMLH>2.0.CO;2.

Vannière, B., E. Guilyardi, G. Madec, F. J. Doblas-Reyes, and
    S. Woolnough, 2013: Using seasonal hindcasts to understand
    the origin of the equatorial cold tongue bias in CGCMs and its
    impact on ENSO. *Climate Dyn.*, **40**, 963–981, https://doi.org/
    10.1007/s00382-012-1429-6.

Vecchi, G. A., and Coauthors, 2014: On the seasonal forecasting of
    regional tropical cyclone activity. *J. Climate*, **27**, 7994–8016,
    https://doi.org/10.1175/JCLI-D-14-00158.1.

Wang, B., and Y. Wang, 1999: Dynamics of the ITCZ–equatorial
    cold tongue complex and causes of the latitudinal climate
    asymmetry. *J. Climate*, **12**, 1830–1847, https://doi.org/10.1175/
    1520-0442(1999)012<1830:DOTIEC>2.0.CO;2.

Watanabe, M., and A. T. Wittenberg, 2012: A method for disen-
    tangling El Niño–mean state interaction. *Geophys. Res. Lett.*,
    39, L14702, https://doi.org/10.1029/2012GL052013.

Wittenberg, A. T., 2015: Low-frequency variations of ENSO. U.S.
    CLIVAR Variations, Vol. 13, U.S. CLIVAR Program Office,
    Washington, D.C., 21–25.

——, A. Rosati, N.-C. Lau, and J. J. Ploshay, 2006: GFDL's
    CM2 global coupled climate models. Part III: Tropical Pacific
    climate and ENSO. *J. Climate*, **19**, 698–722, https://doi.org/
    10.1175/JCLI3631.1.

——, and Coauthors, 2018: Improved simulations of tropical Pa-
    cific annual-mean climate in the GFDL FLOR and HiFLOR
    global coupled GCMs. *J. Adv. Model. Earth Syst.*, https://
    doi.org/10.1029/2018MS001372, in press.

Xue, Y., M. Chen, A. Kumar, Z.-Z. Hu, and W. Wang, 2013: Pre-
    diction skill and bias of tropical Pacific sea surface temperatures
    in the NCEP Climate Forecast System version 2. *J. Climate*, **26**,
    5358–5378, https://doi.org/10.1175/JCLI-D-12-00600.1.

Zheng, Y., J.-L. Lin, and T. Shinoda, 2012: The equatorial Pacific
    cold tongue simulated by IPCC AR4 coupled GCMs: Upper
    ocean heat budget and feedback analysis. *J. Geophys. Res.*,
    117, C05024, https://doi.org/10.1029/2011JC007746.

Zuidema, P., and Coauthors, 2016: Challenges and prospects for
    reducing coupled climate model SST biases in the eastern
    tropical Atlantic and Pacific Oceans: The U.S. CLIVAR
    Eastern Tropical Oceans Synthesis Working Group. *Bull.
    Amer. Meteor. Soc.*, **97**, 2305–2328, https://doi.org/10.1175/
    BAMS-D-15-00274.1.